Effect of subgrid-scale mixing on the evolution of submesoscale instabilities

Sanjiv Ramachandran*

Department of Physics, University of Massachusetts, Dartmouth, MA

Amit Tandon

Department of Physics and Department of Estuarine & Ocean Sciences, University of Massachusetts, Dartmouth, MA

Amala Mahadevan

Woods Hole Oceanographic Institution, Woods Hole, MA

Abstract

We study the effect of subgrid-scale (SGS) mixing on the evolution of a zonal, frontal jet initially in thermal-wind balance with a meridional density gradient and forced by downfront surface winds. The horizontal size of the model domain (O (100 km)) is large enough to contain mesoscale eddies while the horizontal grid resolution (500m) is fine enough to resolve submesoscale eddies. We compare the performance of two subgrid-scale (SGS) models: (i) constant lateral SGS viscosities ($1\mathrm{m}^2\mathrm{s}^{-1}$ and $5\mathrm{m}^2\mathrm{s}^{-1}$) and an analytically prescribed vertical SGS viscosity; and (ii) an existing variant of the original Smagorinsky SGS model developed for anisotropic grids with large aspect ratios. Our simulations show the subgrid model can influence adversely the dynamics at scales of motion far removed from the grid cutoff scale. In particular, we find the following are insufficiently robust to changes in the subgrid model or the model constant for a given subgrid model: (i) the

*Corresponding author

Email addresses: sramachandran@umassd.edu (Sanjiv Ramachandran), atandon@umassd.edu (Amit Tandon), amahadevan@whoi.edu (Amala Mahadevan)

strength of the inverse and forward cascades; (ii) the efficiency of conversion of available potential energy (APE) to eddy kinetic energy (EKE); and (iii) the zonally-averaged resolved-scale EKE budgets. Among the different simulations, those using a constant lateral SGS viscosity of 5 $\mathrm{m^2 s^{-1}}$ exhibit the weakest inverse and forward cascades, and the most inefficient conversion of APE to EKE. Differences in the zonally-averaged resolved-scale EKE budgets obtained using the two SGS models are minimal within a near-surface layer similar to the traditional Monin-Obukhov (MO) layer. Below this MO-like layer, however, the differences are significant as simulations with a constant lateral SGS viscosity and a background SGS vertical viscosity fail to reproduce a realistic balance between the various terms in the EKE budget. A lateral viscosity of 1 $\mathrm{m^2 s^{-1}}$ predicts the production of EKE is balanced solely by pressure transport with negligible SGS destruction, whereas recent experimental studies show enhanced destruction near fronts. For a constant lateral viscosity of 5 $\mathrm{m^2 s^{-1}}$ the magnitude of the dominant production term is an order of magnitude smaller than scaling estimates in the literature due to the poor conversion of APE to EKE. The EKE budgets obtained using the anisotropic Smagorinsky model (ASM) show production of EKE is balanced by a combination of pressure transport and SGS destruction. The magnitude of the dominant production term is consistent with existing scaling estimates in the literature.

Keywords: Subgrid model, Subgrid viscosity, Submesoscale, Smagorinsky, Anisotropic grid

1. Introduction

In the ocean, submesoscales are scales of motion smaller than the Rossby radius of deformation but large enough to be influenced by planetary rotation (Thomas et al., 2007). Numerical studies show oceanic density-fronts are active sites of submesoscale instabilities (Capet et al., 2008c,a,b; Fox-Kemper et al., 2008; Klein et al., 2008; Mahadevan, 2006; Mahadevan and Tandon, 2006) which occur in strongly frontogenetic regions associated with O(1) Rossby number (Ro), thereby creating conditions suitable for departure from balanced dynamics (Molemaker et al., 2010; Molemaker and McWilliams, 2005). The O(1) Ro implies the dynamics at the submesoscales is not amenable to classical quasi-geostrophic (QG) analysis which assumes $Ro \ll 1$ (Pedlosky, 1987).

A case study considered often in the literature and in some of the studies cited above is the evolution of a density front forced by downfront surface winds, which create loss of balance by destroying potential vorticity (PV) near the surface (Thomas, 2005) (Downfront winds are winds aligned with the frontal jet in thermal-wind balance with the lateral density gradient). In simulations such systems spawn submesoscale motions with O(100 m/day) vertical velocities at the frontal edges (Mahadevan, 2006). Such rapid vertical motions can accomplish the transport of nutrients from the ocean interior to the surface on inertial time-scales and thus, could be an important factor governing phytoplankton production in the upper ocean (Lévi et al., 2001; Mahadevan and Archer, 2000).

Submesoscales play a central role in the downscale transfer of energy from the O(100 km) mesoscales to scales O(0.1–100 m), associated with three-dimensional isotropic turbulence. The mesoscales exhibit an inverse cascade of energy, on average, consistent with the quasi-geostrophic (QG) framework (Charney, 1971; McWilliams et al., 1994) while small-scale turbulence exhibits a forward cascade of energy, on average (Tennekes and Lumley, 1972). Submesoscale instabilities, by enabling forward cascades of energy in localized regions of unbalanced dynamics, create pathways for the local removal of mesoscale energy in the ocean interior (Capet et al., 2008b; McWilliams, 2003), away from the boundaries.

Theory and numerical experiments (Boccaletti et al., 2007; Fox-Kemper et al., 2008; Fox-Kemper and Ferrari, 2008) show submesoscale baroclinic instabilities significantly enhance the rate of restratification of the mixed layer (ML), thereby weakening the basis for one-dimensional mixing parameterizations near density fronts. The stratification arising due to these instabilities can be an order of magnitude larger than that due to geostrophic adjustment alone (Mahadevan et al., 2010; Tandon and Garrett, 1994).

Past numerical studies of oceanic submesoscales can be divided crudely into one of two categories: (i) Simulations in computational domains that contain and resolve both mesoscale and submesoscale features, but are too coarse to resolve the smaller, turbulent scales; and (ii) Large-eddy simulations (LES) in smaller domains with grid resolutions fine enough to resolve the turbulent scales. The former category is suitable for studying the evolution and coupling of meso- and submeso-scales whereas the latter is ideal for identifying mechanisms that trigger a forward cascade of energy to the smaller, isotropic scales associated with three-dimensional turbulent mixing. In the first category are studies by Mahadevan (2006), Mahadevan and Tandon (2006), Thomas et al. (2007), Capet et al. (2008c,a,b), Fox-Kemper et al. (2008) and Klein et al. (2008). These authors employed domains that are O(100 km) in the horizontal and O(100 m–1 km) in the vertical with corresponding grid resolutions of O(500 m–1 km), and O(1-10 m)[1], respectively. Our present study belongs in this category. The second category includes LES by Ozgokmen et al. (2011), Skyllingstad and Samelson (2011), Taylor and Ferrari (2009) and Taylor and Ferrari (2010) among others. These authors use domains that are O(1–10 km) in the horizontal and O(100 m) in the vertical with isotropic grids having O(1 m) resolution. The LES studies have grid resolutions fine enough to resolve three-dimensional turbulent motions and some of them (Skyllingstad and Samelson, 2011) use domains large enough to contain one O(6 km) baroclinic eddy.

Both classes of simulations described above are different from the so-called MOLES (Fox-Kemper and Menemenlis, 2008), or Mesoscale Ocean Large-Eddy Simulations, where the grid resolution is fine enough to resolve the mesoscale kinetic energy spectrum but too coarse to resolve submesoscales. In MOLES, the grid-scale is associated necessarily with an inverse cascade of energy, on average, whereas in submesoscale-resolving simulations the transfer of energy switches from an inverse to forward cascade (on average) at scales larger than the grid-scale (Capet et al., 2008b; Klein et al., 2008). This suggests such simulations—unlike MOLES—might be compatible with traditional LES subgrid closures which typically (but not always) are designed to ensure a net forward cascade of energy from the resolved to the

[1] This refers to the near-surface vertical resolution as these studies typically use a vertically stretched grid.

subgrid scales of motion (Fox-Kemper and Menemenlis, 2008).

Here, we explore the performance of an anisotropic Smagorinsky subgrid-scale (SGS) model (Roman et al., 2010) in submesoscale-resolving simulations performed with the Process Study Ocean Model (PSOM, Mahadevan (2006)). Fox-Kemper et al. (2008) used the Smagorinsky model (Smagorinsky, 1963) to parameterize lateral SGS mixing in conjunction with a constant background vertical SGS viscosity. The anisotropic variant developed by Roman et al. (2010) prescribes both lateral and vertical SGS viscosities (and diffusivities). Furthermore, it accommodates anisotropic grids and hence is suitable for our simulations where the horizontal grid resolution is much coarser than the vertical grid resolution. We simulate a front forced by downfront winds and contrast the results obtained using the anisotropic Smagorinsky model (ASM) with those obtained using constant lateral SGS viscosities and an analytically prescribed vertical SGS viscosity. As part of the comparison, we emphasize differences that bear directly on the temporal evolution of the large-scale features of the flow. In a recent study, Marchesiello et al. (2011) investigated the submesoscale dynamics in tropical instability waves of the Pacific ocean using a series of simulations at different resolutions that explicitly set lateral SGS mixing to zero and model vertical SGS mixing using the K-Profile Parameterization (Large et al., 1994). They found the effects of numerical mixing are significant at wavenumbers well below the grid-cutoff wavenumber which implies the effective resolution of the simulation is lesser than that allowed by the grid. In this study, we show the effective resolution also depends on both the type of SGS model and the choice of model constants for a given SGS model.

1.1. Outline

In Sections 2.1 and 2.2 we describe briefly the model equations in PSOM and the SGS model, respectively. Section 3 describes the initial conditions and the set-up of the numerical simulations. We discuss results in Section 4 and summarize our conclusions in Section 5.

2. Modelling

For notational ease we switch between the indexed and the conventional representation of variables when necessary. For instance, the symbols $\{x_i, (i = 1, 2, 3)\}$ and (x, y, z) are equivalent as are $\{u_i, (i = 1, 2, 3)\}$ and (u, v, w).

2.1. Model equations

The Process Study Ocean Model, or PSOM, is a three-dimensional (3D), non-hydrostatic model (Mahadevan, 2006). In what follows, variables with the tilde operator represent filtered (resolved-scale) variables and those without the tilde operator represent unfiltered fields. We use the words resolved (or resolved-scale) and filtered interchangeably in this document. The unfiltered fields contain information across the entire range of length scales down to the Kolmogorov microscale (Tennekes and Lumley, 1972). Only the filtered fields are available because a discrete computational grid cannot resolve scales of motion finer than the grid resolution. The nonlinearity of the Navier-Stokes equations, however, gives rise to subgrid-scale terms that need to be modeled to close the system of equations for the filtered variables[2].

[2]Except in a Direct Numerical Simulation (DNS) where the grid resolution is fine enough to resolve the Kolmogorov microscale, obviating the need for an SGS model

The model equations in non-dimensional form are:

$$D_t\tilde{\rho} = \tilde{F}^{\tilde{\rho}} - \frac{\partial \tau_i^{\rho}}{\partial x_i} \tag{1}$$

$$D_t\tilde{u} + Ro^{-1}\big(\tilde{p}_x + \gamma\tilde{q}_x^* - f\tilde{v} + Ro\,\delta\,b\tilde{w}\big) = \tilde{F}^x - \frac{\partial \tau_{ij}^d}{\partial x_j} \;\; ; \;\; i = 1 \tag{2}$$

$$D_t\tilde{v} + Ro^{-1}\big(\tilde{p}_y + \gamma\tilde{q}_y^* + f\tilde{u}\big) = \tilde{F}^y - \frac{\partial \tau_{ij}^d}{\partial x_j} \;\; ; \;\; i = 2 \tag{3}$$

$$D_t\tilde{w} + Ro^{-2}\,\delta^{-1}\left(\frac{\gamma}{\delta}\tilde{q}_z^* - b\tilde{u}\right) = \tilde{F}^z - \frac{\partial \tau_{ij}^d}{\partial x_j} \;\; ; \;\; i = 3 \tag{4}$$

$$\tilde{u}_x + \tilde{v}_y + Ro\,\tilde{w}_z = 0, \tag{5}$$

where $D_t \equiv \partial_t + \tilde{u}\partial_x + \tilde{v}\partial_y + Ro\,\tilde{w}\partial_z$ is the non-dimensional material derivative operator. The variables $\tilde{u}$, $\tilde{v}$ and $\tilde{w}$ denote the non-dimensional filtered velocity components along the eastward (x), northward (y) and upward (z) directions, respectively, on the earth's surface. The variable $\tilde{\rho}$ denotes the filtered density perturbation from the background stratification prescribed at $t = 0$. The components of the Coriolis acceleration scaled with the earth's angular velocity, Ω, are denoted by $f = 2\sin(\phi)$ and $b = 2\cos(\phi)$ where ϕ is the latitude. Defining U, W, L and D to be the relevant scales for the horizontal velocity, vertical velocity, the horizontal and vertical length scales, respectively, the non-dimensional parameters in the model are: (i) the Rossby number, $Ro = U/\Omega L$, where Ω is the angular velocity of rotation of the earth; (ii) ratio of the non-hydrostatic (NH) to hydrostatic (HY) pressure variations, $\gamma = Q/P$, where Q and P are the characteristic scales for the NH and HY components, respectively; and (iii) the aspect ratio, $\delta = D/L$. For the NH runs, it is appropriate to set $\gamma = \delta$ (Mahadevan, 2006). The filtered HY component is denoted by $\tilde{p}$ and the filtered, modified NH component (discussed below) by $\tilde{q}^*$. Setting $\gamma = 0$ turns off the NH effects. By definition, $\tilde{p}$ satisfies $\tilde{p}_z + \tilde{\rho} g = 0$, where g is the acceleration due to gravity. Scaling the vertical vorticity equation and assuming a balance between the advection and divergence terms yields $W = Ro\,\delta\,U$ (Mahadevan, 1996).

The filtered forcing terms are shown on the right hand side of (1)—(4) as $\tilde{F}^\rho$, $\tilde{F}^x$ and so on. We assume implicitly the forcing terms are described completely by their filtered parts, i.e., they lack spatial structure finer than the grid resolution. The non-dimensional SGS density fluxes are denoted by $\tau_i^\rho = \widetilde{\rho u_i} - \tilde{\rho}\tilde{u}_i$. We denote the deviatoric non-dimensional SGS momentum stress tensor as $\tau_{ij}^d = \widetilde{u_i u_j} - \tilde{u}_i\tilde{u}_j - (2/3)\delta_{ij}e_{\text{sgs}}$, where δ_{ij} is the Kronecker-Delta operator and $e_{\text{sgs}} = \widetilde{u_i u_i} - \tilde{u}_i\tilde{u}_i$ is the non-dimensional SGS kinetic energy. By construction, τ_{ij}^d is traceless. The variable $\tilde{q}^*$ is the modified, filtered NH component of pressure as it includes a contribution from $(2/3)e_{\text{sgs}}$, in addition to the true NH pressure component. To solve for the filtered fields in (1)—(5), we must parameterize the three SGS fluxes and the six independent SGS stresses. Knowledge of the SGS kinetic energy requires an additional parameterization for e_{sgs}, which we do not undertake in this study.

2.2. Subgrid model

Lilly (1967) first tuned the Smagorinsky subgrid model (SM, Smagorinsky (1963)) to dissipate the "correct" amount of energy in homogeneous, isotropic, 3D turbulence assuming the grid-cutoff wavenumber lies within the inertial subrange. The value of the Smagorinsky model constant Lilly derived is not meant to be universal due to the assumptions underlying his derivation. For instance, it is not valid for strongly anisotropic turbulence or when the grid resolution is too coarse to resolve the inertial subrange. Germano et al. (1991) developed the Dynamic Smagorinsky model (DSM) which prescribes the subgrid model constant as a function of space and time by relating the resolved-scale fields filtered at two different scales through the Germano identity (Germano et al., 1991). This dynamic evaluation of the subgrid model constant enables the DSM, in principle, to exhibit negative eddy-viscosities and thus, backscatter, or, the transfer of energy from the subgrid to the resolved scales. In practice, negative eddy-viscosities give rise to numerical instabilities (Lilly, 1992) and are usually clipped, effectively eliminating backscatter. Both DNS (Piomelli et al., 1991) and field measurements (Sullivan et al., 2003) of 3D turbulence show significant amounts of backscatter with a slightly stronger forward cascade to yield a *net* forward (downscale) cascade of energy at the grid scale (Tennekes and Lumley, 1972). The SM, by construction, permits only a downscale transfer of energy from the resolved to the subgrid scales, at every single grid point. When the grid scale lies within the submesoscales, where the flow regime is considerably different from 3D, isotropic turbulence, it is unclear what are the relative fractions of grid-scale forward and inverse cascades, although simulations show an onset of a forward cascade, on average, at scales O(10km) (Capet et al., 2008b). The DSM model has been used successfully in past LES studies of oceanic flows (Ozgokmen et al., 2009, 2011; Tejada-Martínez, 2009) with nearly isotropic grids. Scotti and Meneveau (1993), and Scotti et al. (1997) modified the SM and the DSM for anisotropic grids by obtaining analytical expressions for the subgrid model constant as a function of the grid anisotropy, assuming the grid spacings in all three directions lie in the inertial subrange.

Simulations designed to study the simultaneous evolution of both mesoscale meanders and submesoscale features in the ocean typically use anisotropic grids, as the vertical resolution, Δz, is much finer than the horizontal resolution, Δx (or Δy), due to the large aspect ratio of the domains, with horizontal scales much larger than the vertical scales (Capet et al., 2008c; Klein et al., 2008; Mahadevan, 2006). Roman et al. (2010) developed an anisotropic Smagorinsky model (ASM) that derives from past work by Kamenkovich (1977), Miles (1994) and Wajsowicz (1993), and is designed for grids where $\Delta x \gg \Delta z$. Owing to the highly anisotropic grids and coarse resolutions[3] in our simulations, we use the SGS model designed by Roman et al. (2010). ASM does not require the grid resolution to belong in the inertial subrange, but this generality comes at a cost, namely, the lack of analytical expressions relating the subgrid model constants to the grid anisotropy.

Let us denote the dimensional eddy-viscosity tensor by K_{ij}, which is assumed to be symmetric. ASM reduces the six independent components to three: $K_{11} = K_{12} = K_{22}$, $K_{13} = K_{23}$ and K_{33}. In the discussion below, we use upper-case symbols for dimensional variables. The three independent components are given by:

$$K_{11} = (c_1 \Delta x)^2 |\widetilde{S}_h| \ \ ; \ \ K_{13} = (c_2 \Delta z)^2 |\widetilde{S}_v| \ \ ; \ \ K_{33} = (c_3 \Delta z)^2 |\widetilde{S}_r|, \qquad (6)$$

where the dimensional, filtered strain rates $\widetilde{S}_h$, $\widetilde{S}_v$ and $\widetilde{S}_r$ are defined as

[3]Insufficient to resolve the inertial subrange

follows:

$$|\widetilde{S}_h| = \sqrt{2\big(\widetilde{S}_{11}^2 + \widetilde{S}_{22}^2 + \widetilde{S}_{12}^2\big)} \tag{7}$$

$$|\widetilde{S}_v| = \sqrt{4\widetilde{S}_{13}^2 + 4\widetilde{S}_{23}^2} \tag{8}$$

$$|\widetilde{S}_r| = \sqrt{2\widetilde{S}_{33}^2}. \tag{9}$$

In (7)—(9) the filtered strain-rate tensor $\widetilde{S}_{ij} = 0.5\big(\partial\tilde{U}_i/\partial\tilde{X}_j + \partial\tilde{U}_j/\partial\tilde{X}_i\big)$ where $\tilde{U}_i$ is the dimensional ith component of velocity and $\tilde{X}_i$ is the dimensional ith coordinate. The stress divergence terms in the dimensional horizontal momentum equations are (Roman et al., 2010),

$$\frac{\partial}{\partial\tilde{X}_1}\big(2K_h\widetilde{S}_{i1}\big) + \frac{\partial}{\partial\tilde{X}_2}\big(2K_h\widetilde{S}_{i2}\big) + \frac{\partial}{\partial\tilde{X}_3}\big(2K_v\widetilde{S}_{i3}\big) \quad ; \quad i = 1, 2, \tag{10}$$

where $K_h = K_{11}$ and $K_v = K_{13}$. The stress divergence terms in the dimensional vertical momentum equation are,

$$\frac{\partial}{\partial\tilde{X}_1}\big(2K_v\widetilde{S}_{i1}\big) + \frac{\partial}{\partial\tilde{X}_2}\big(2K_v\widetilde{S}_{i2}\big) + \frac{\partial}{\partial\tilde{X}_3}\big(2K_r\widetilde{S}_{i3}\big) \quad ; \quad i = 3, \tag{11}$$

where $K_r = K_{11} - 2K_{13} + 2K_{33}$ (Roman et al., 2010). The eddy-diffusivities, K_i^ρ, are computed assuming a constant eddy Prandtl number, Pr_e, such that the horizontal components $K_1^\rho = K_2^\rho = Pr_e^{-1}K_h$ and the vertical component $K_3^\rho = Pr_e^{-1}K_v$. The constant-Pr_e assumption is one of convenience and lacks a rigorous basis (Moeng and Wyngaard, 1988) but is invoked frequently in LES studies due to its simplicity (Harcourt and D'Asaro, 2008; Sullivan et al., 2007; Taylor and Ferrari, 2010). Roman et al. (2010) use $Pr_e = 0.5$, while some LES studies use a value of 1 (Harcourt and D'Asaro, 2008; Taylor and Ferrari, 2010). We will assume $Pr_e = 1$ in all our simulations. For the value of Ro used in our simulations (discussed in Section 3) the third term in (11) scales as an order of magnitude smaller than the other two terms in the equation. Hence, to simplify our subgrid parameter space, we further impose $c_2 = c_3$ in all our runs, that leaves two free SGS parameters, c_1 and c_2

We now explain a modification to the ASM in our simulations. In the formulation by Roman et al. (2010) there is no dependence on the Richardson number, Ri, in (6) which implies vertical mixing (of momentum or density) regardless of the underlying stratification. To suppress such unphysical mixing Ozgokmen et al. (2007) multiplied the vertical components of the eddy-viscosity and/or eddy-diffusivity by the following function (Ozgokmen et al., 2007):

$$f(Ri) = \begin{cases} 1 & Ri < 0 \\ \sqrt{1 - \frac{Ri}{Ri_c}} & 0 \leq Ri \leq Ri_c = 0.25 \\ 0. & Ri > Ri_c \end{cases} \tag{12}$$

The function in (12) turns off the vertical mixing when Ri exceeds a critical value, $Ri_c = 0.25$, above which the stratification is considered too strong to sustain continuous turbulence. The correction factor in (12) is empirical and neglects patchy, intermittent mixing for $Ri_c > 0.25$ (Ohya et al., 2008). Ozgokmen et al. (2007) found the Ri-based correction works best when it is applied only to the vertical SGS diffusivity but not to the vertical SGS viscosity. Thus, we restrict the use of the correction factor in (12) to K_ρ. In their LES studies of the dam break problem Ozgokmen et al. (2007) found such a Ri-based correction with $Ri_c = 0.25$ (Miles, 1961) improved the performance of the classic Smagorinsky model significantly.

3. Numerical Experiments

In this section, we outline briefly the physical parameters in our numerical simulations which follow those in the study by Mahadevan (2006).

We use the following values for the three non-dimensional parameters in (2)–(4): (i) $\delta = 10^{-2}$; (ii) $Ro = 0.1$; and (iii) $\gamma = \delta$.

3.1. Domain, forcing and boundary conditions

The domain dimensions are $L_x = 96$ km (zonal), $L_y = 192$ km (meridional) and $L_z = 500$ m (vertical). The computational grid has 192, 384 and 32 points in the zonal, meridional and vertical directions, respectively, which corresponds to a constant horizontal grid spacing of 500 m. A stretched vertical coordinate yields a resolution of 3.6m at the surface and 35m at the bottom, assumed to be a flat surface.

We impose downfront, westerly (West to East, or W–E) surface-winds that vary sinusoidally in the meridional direction (Fig 2, bottom panel). The amplitude of the sinusoidally varying, zonal surface wind-stress, τ_x, increases linearly from zero to its maximum value of 0.1 N m^{-2} over a day. The downfront winds attempt to restore the front by advecting heavier over lighter fluid due to Ekman transport (Thomas, 2005). The ML eddies tend to restratifiy the fluid by converting the APE to kinetic energy (Fox-Kemper et al., 2008). The simulation parameters determine whether there is net restratification, net destratification or a dynamic equilibrium between the restratifying and destratifying mechanisms (Mahadevan et al., 2010).

The boundary conditions are periodic in the E–W direction. The south and the north boundaries are impermeable walls across which we impose zero advective fluxes and zero meridional gradients of the velocity, density and, SGS fields. The SGS stresses τ_{13}^d and τ_{23}^d at the free-surface satisfy $\tau_x/\rho_0 = \tau_{13}^d$ and $\tau_y/\rho_0 = \tau_{23}^d$, where τ_y is the meridional surface wind-stress (zero in this study) and $\rho_0 = 1027$ kg m^{-3} is the reference density. The SGS flux τ_3^ρ at the surface is set equal to the surface density flux, which in this study is zero due to the absence of cooling or heating at the surface. We model bottom friction using a linear drag, $r_{\text{bot}}(U, V)$, where the constant bottom friction coefficient $r_{\text{bot}} = 5 \times 10^{-4}$ s^{-1} and (U, V) are the dimensional horizontal velocities.

The topmost layer of grid cells follow the free-surface (Mahadevan, 1996). The reference Coriolis parameter $f_0 = 1 \times 10^{-4}$ s^{-1}. The time step of integration is 216 seconds.

3.2. Initial conditions

We prescribe a south-to-north (S–N) density gradient confined to the mixed layer and in thermal-wind balance with a westerly jet, as shown in Fig. 1. The initial mixed layer depth (MLD) is 105 m. The top panel of Fig. 2 shows the initial profiles of buoyancy frequency, N^2, and the potential density, ρ, at the front. The variable N^2 assumes a uniform value of 10^{-6} s^{-2} within the ML, which reaches a maximum $\approx 3 \times 10^{-4}$ s^{-2} through the pycnocline and is constant at 1.5×10^{-6} s^{-2} below the pycnocline. The middle panel in Fig. 2 shows the free-surface elevation and the meridional variation of the meridional buoyancy gradient, $\partial b/\partial y$ at a depth of 50 m, where $b = -(g/\rho_0)(\tilde{\rho} - \rho_0)$ is the buoyancy. The peak magnitude of the meridional buoyancy gradient is 0.9×10^{-7} s^{-2}. We do not restore the S–N density gradient which implies our simulations do not have a fixed reservoir of APE. The higher elevation of the free surface on the lighter side ensures

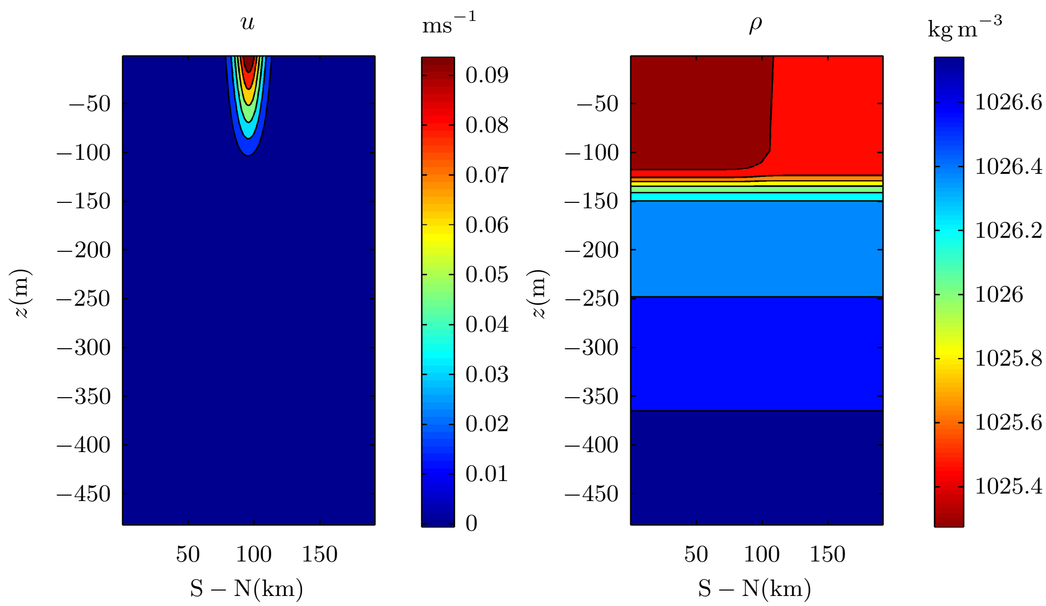

Figure 1: The initial potential density field is in thermal-wind balance with a westerly geostrophic jet confined to the mixed layer. The level of no motion lies at $z = -105$m, the bottom of the ML.

the initial barotropic and baroclinic pressure gradients at the bottom of the ML are equal and opposite. To nudge the onset of instabilities the density front has an initial wiggle in the form of a sinusoidal wave whose amplitude is 100 m and wavelength is equal to the zonal extent of the domain.

3.3. Constant SGS lateral viscosities

For comparison we also present results obtained using constant lateral SGS viscosities (and diffusivities), denoted by K_x and K_y, and a vertical SGS viscosity, K_v, prescribed analytically using a hyperbolic tangent profile (Mahadevan, 2006). We use two values of K_x ($= K_y$): 1 m^2 s^{-1} and 5 m^2 s^{-1} while K_v, which remains unchanged for both K_x values, varies smoothly

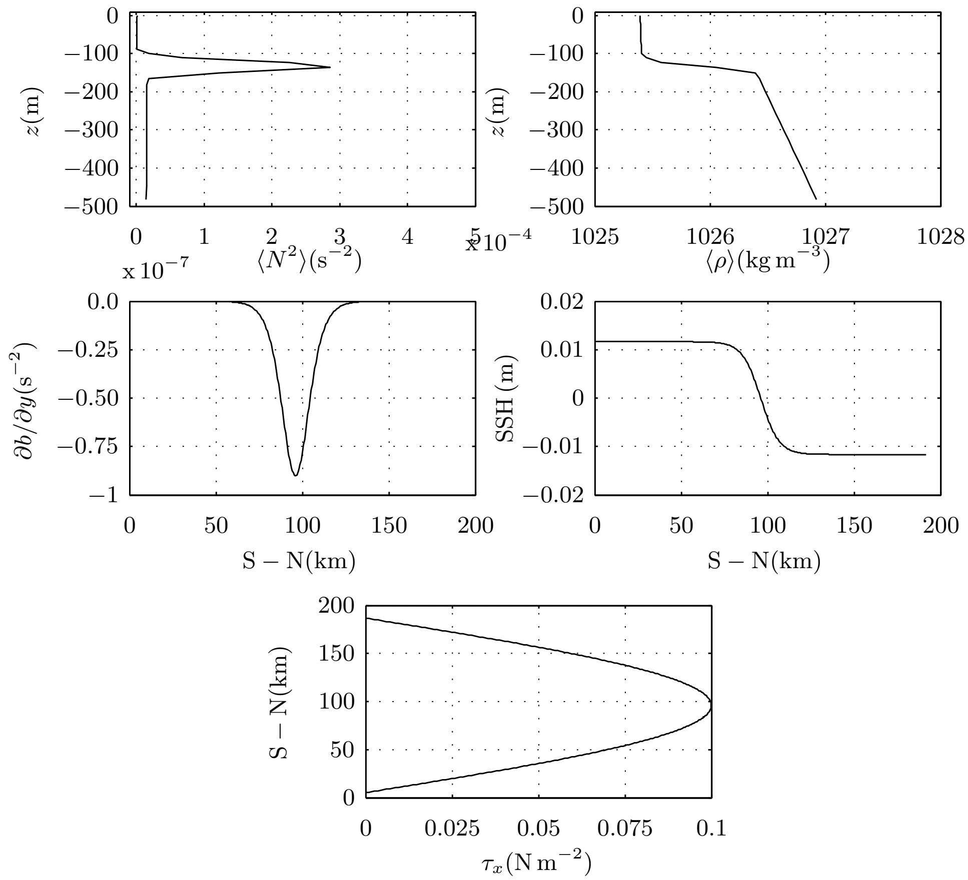

Figure 2: Top panel: Initial vertical profiles of N^2 (s^{-2}) and ρ (kgm^{-3}) at $y = 96$km. Middle panel: Initial meridional variation of the lateral buoyancy gradient, $\partial b/\partial y$ (s^{-2}), at a depth of 50 m and of the free-surface elevation (in metres). Bottom panel: Meridional variation of zonal wind-stress (after initial ramping up), showing a sinusoidal profile with an amplitude of 0.1 Nm^{-2}.

from 10^{-3} m^2 s^{-1} within the Ekman layer (depth = $(0.4/f)(\tau_x/\rho_0)^{1/2}$) to a background value of 10^{-5} m^2 s^{-1} in the interior.[4]

Roman et al. (2010) tuned their SGS constants by examining low-order velocity statistics in simulations of plane channel flow. While we show plots for a few representative values of the SGS constants, we do not attempt here to identify the "optimal" SGS constants. Such an undertaking requires a systematic investigation of the interplay between the grid aspect ratio and the SGS constants (Brasseur and Wei, 2010), which is beyond the scope of this study. Instead, we examine whether there are significant differences in the results obtained using the ASM and those obtained using a subgrid model with constant lateral subgrid viscosities.

4. Results

4.1. Instantaneous fields

Snapshots of the near-surface density and velocity fields after $t = 20T_f$ (Fig. 3 and 4), where $T_f = 2\pi/f_0$ is one inertial period, show the front has undergone baroclinic instability and developed meanders whose edges exhibit submesoscale features. There are, however, noticeable differences between the run with $K_x = 5$ m^{2}s^{-1} and the other two simulations. In the former, the submesoscale features and the frontal meanders are weaker than in the latter two simulations. In later sections, we show this is related to weaker frontogenesis and inefficient conversion of APE to kinetic energy for $K_x = 5$ m^{2}s^{-1} compared to the other two cases. Snapshots of vertical velocity (Fig. 4) show strong vertical motions near the frontal edges with upwelling on

[4]This implies K_v assumes the background value everywhere in the domain in the absence of surface winds.

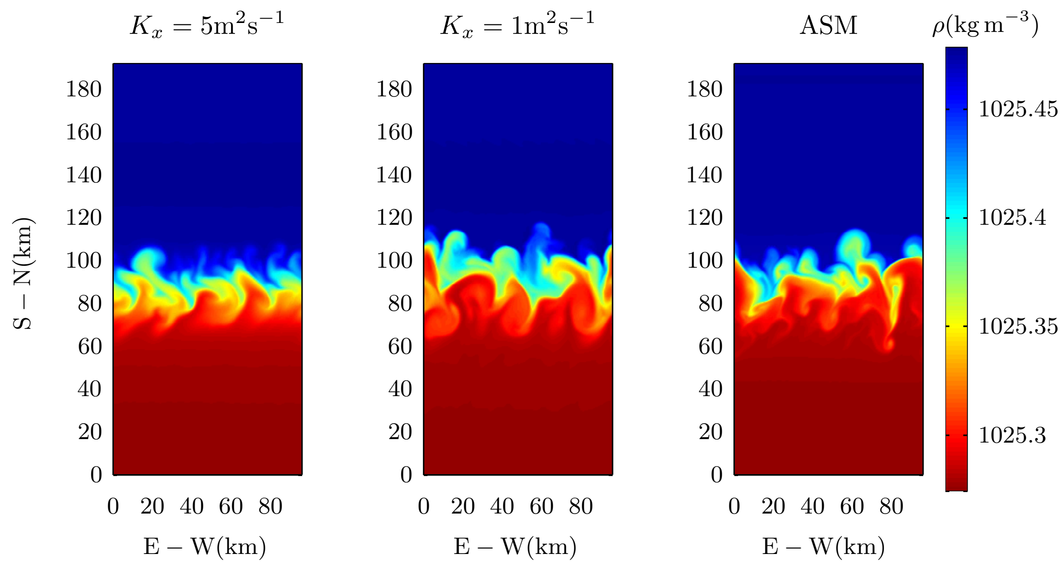

Figure 3: Snapshots of the near-surface ($z = -10$ m) potential density field at $t = 20T_f$, where $T_f = 2\pi/f_0 = 17.5$ hours is one inertial period, for runs with $K_x = 5\ \mathrm{m}^2\mathrm{s}^{-1}$, $K_x = 1\ \mathrm{m}^2\mathrm{s}^{-1}$ and the Anisotropic Smagorinsky model.

the lighter side of the front and downwelling on the denser side, suggestive of a thermally direct circulation induced by the ML eddies. Downwelling is stronger than upwelling and occurs in narrower streaks of length O(10 km) and width O(1 km). For the ASM, the peak negative velocities ($\approx$ 120 m/day) are much larger than the peak positive velocities ($\approx$ 50 m/day). This asymmetry is also present in simulations with $K_x = 1\ \mathrm{m}^2\mathrm{s}^{-1}$ and to some extent for $K_x = 5\ \mathrm{m}^2\mathrm{s}^{-1}$. The difference in the peak upwelling and downwelling velocities was also reported in previous studies (Capet et al., 2008c; Klein et al., 2008; Mahadevan, 2006).

Unlike ASM, the runs with constant K_x exhibit strong wave-like features north and south of the front with intense upwelling and downwelling along narrow streaks near the front. The waves disappear for still higher values of K_x (≈ 10 m^{2}s^{-1}) (not shown). The runs with the ASM also yield wave-like structures to the north and the south of the front but with much lesser amplitudes. One consequence of these waves is the transport of kinetic energy generated near the front. At equilibrium, in the absence of significant advection, we expect the sum of the energy transported away from the front and that dissipated locally equals the total energy input from the surface winds. As the imposed surface winds are identical in all our simulations we expect lower levels of local dissipation through the SGS model to be compensated by larger wave-induced transport of energy. In later sections we analyze the eddy kinetic energy budgets and relate the presence of the oscillatory features in Fig. 4 to weaker levels of SGS dissipation.

Snapshots of the near-surface SGS viscosity component, K_{11}, at $t = (7, 14, 20)T_f$ (Fig. 5) reveal a horizontal structure evidently related to that of the potential density field (Fig. 3). The maximum values of K_{11} are approximately 5 m^{2}s^{-1} and occur along the meandering edges of the front associated with high strain rates. Plots of zonally averaged profiles of K_1 and K_{13} near the front show they attain mean values O(1) m^{2}s^{-1} and O(10^{-2}) m^{2}s^{-1}, respectively. The high mean values of K_{13} near the base of the mixed layer are associated with local zonal streaks of alternating positive and negative shear that approximately cancel each other upon averaging zonally.

4.2. Spectra and spectral fluxes

Near-surface zonal spectra of u and ρ for different SGS constants at $t = 15T_f$ (Fig. 7, top panel) exhibit a slope of -2 approximately over a wavenumber range that varies with the value of the subgrid constant.

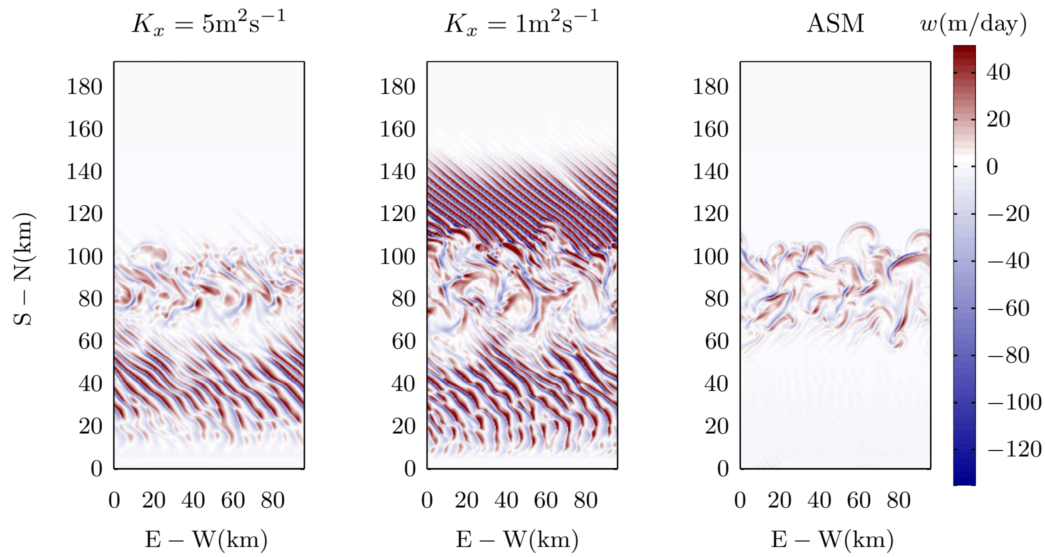

Figure 4: Snapshots of the near-surface ($z = -10$ m) vertical velocity field at $t = 20T_f$, where $T_f = 2\pi/f_0 = 17.5$ hours is one inertial period, for runs with $K_x = 5$ m^{2}s^{-1}, $K_x = 1$ m^{2}s^{-1} and the Anisotropic Smagorinsky model.

For $(c_1, c_2) = (0.25, 0.25)$, this range exists for 3×10^{-4}rad m^{-1} $< \kappa_x <$ 10^{-3}rad m^{-1}, or length scales 6–20 km ($2\pi/\kappa_x$). A slope of -2 at intermediate scales is consistent with previous numerical studies (Capet et al., 2008b; Klein et al., 2008). The higher values of the SGS constants lead to increasingly steeper slopes at the high wavenumbers and a narrowing of the wavenumber range where the spectral slope is -2, a consequence of increased SGS dissipation.

We infer the direction of energy flux from the spectral flux, $\Pi(\kappa_x)$, plotted versus the zonal wavenumber (Fig.7, bottom panel). At the large scales, the spectral flux is negative implying an inverse cascade of energy. It is positive for $\kappa_x > 6 \times 10^{-4}$rad m^{-1} ($<$ 10.5 km), indicative of a downscale transfer

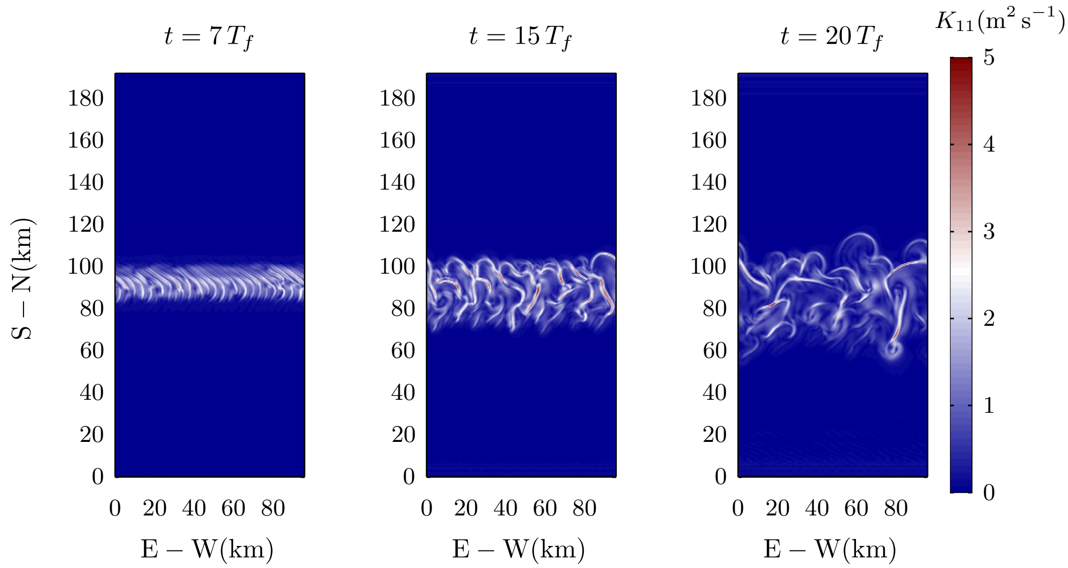

Figure 5: Near-surface ($z = -10$ m) evolution of K_{11}.

of energy at those scales. Capet et al. (2008b) found the transition from an inverse to a forward cascade occurs at $\kappa_x \approx 3 \times 10^{-4}$rad m^{-1}.

Unlike the velocity spectra the spectral flux changes appreciably with varying SGS constants, exhibiting a spread of nearly 50% at the large scales. With increasing SGS dissipation we see a sharp decrease in the peak negative magnitude of $\Pi(\kappa_x)$, implying a decrease in the strength of the inverse cascade. For instance, both the inverse and forward spectral fluxes for $(c_1, c_2) = (0.25, 0.50)$ are negligible. The corresponding spectra and spectral flux for $K_x = 1$ m^{2}s^{-1} (Fig. 8) are qualitatively similar to those for the ASM (Fig. 7), showing an inverse cascade at the larger scales and a forward cascade for $\kappa_x > 6 \times 10^{-4}$rad m^{-1}. For $K_x = 5$ m^{2}s^{-1} (Fig. 8), however, both the inverse and forward cascades are diminished strongly and the spectral

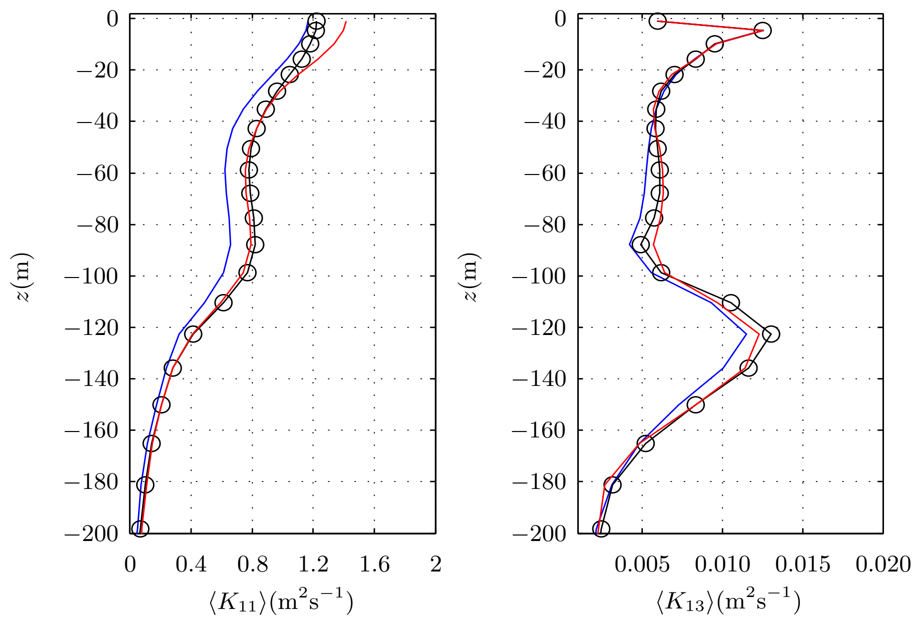

Figure 6: Zonally-averaged profiles of K_{11} and K_{13} at $t = 15T_f$, where $T_f = 2\pi/f_0 = 17.5$ hours is one inertial period. The profiles are averages over one inertial period centered at $t = 15T_f$. The three colours represent meridional sections at $y = y_f$ and $y = y_f \pm 2.5$ km, where $y_f = 96$ km marks the initial location of the front. The circles on the green curve denote the vertical grid levels.

flux is nearly coincident with the zero-line (shown in black). As the inverse cascade is driven by the onset of baroclinic instability, Fig. 7 and 8 suggest a value of $K_x = 5$ m^{2}s^{-1} suppresses the conversion of APE to kinetic energy (discussed in the next section). They show neither the inverse nor the forward cascades need be robust to a change in the SGS model or to changes in the model constant for a given SGS model. The sensitivity of the spectral flux at the largest scales to the SGS model constant shows the influence of the SGS model on scales of motion much larger than the grid-cutoff.

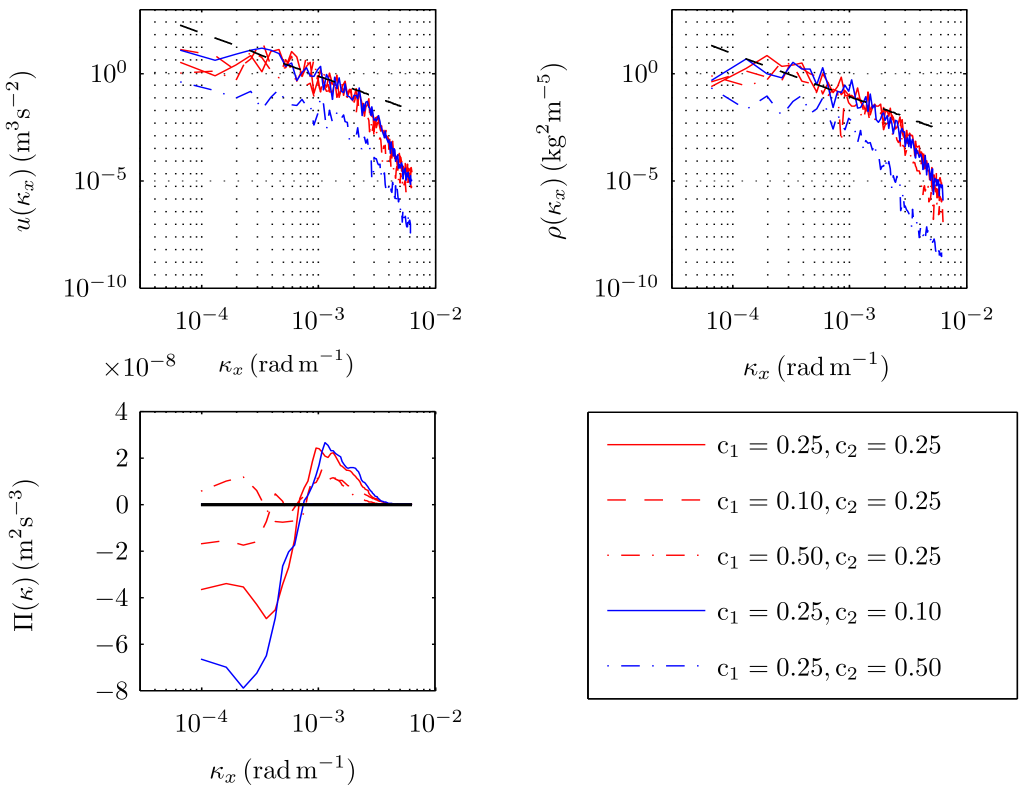

Figure 7: Top panel: Log-log plot showing near-surface spectra (at $z = -4.5$ m) plotted versus zonal wavenumber, κ_x (rad m^{-1}), at $y = 96$km and $t = 15T_f$, where $T_f = 2\pi/f_0 =$ 17.5 hours is one inertial period. The dashed line has a slope of -2. Top left: Zonal velocity spectra, Top right: Potential density spectra. Bottom panel: Spectral flux, $\Pi(\kappa)$ (m^2 s^{-3}) plotted versus zonal wavenumber in a linear-log plot. The different curves denote different combinations of SGS constants. The spectral flux for $c_1 = 0.25, c_2 = 0.50$ (dash-dot line in blue) has much smaller magnitudes and is nearly coincident with the zero line. The spectra and spectral fluxes are averages over one inertial period centered at $t = 15T_f$. A wavenumber of 10^{-3} rad m^{-1} corresponds to a length scale of $2\pi/10^{-3}$ m, or 6.28 km.

4.3. Extraction of APE

Analytical arguments show maximum extraction of APE occurs when the parcels exchange buoyancy along a direction half the isopycnal slope (Haine

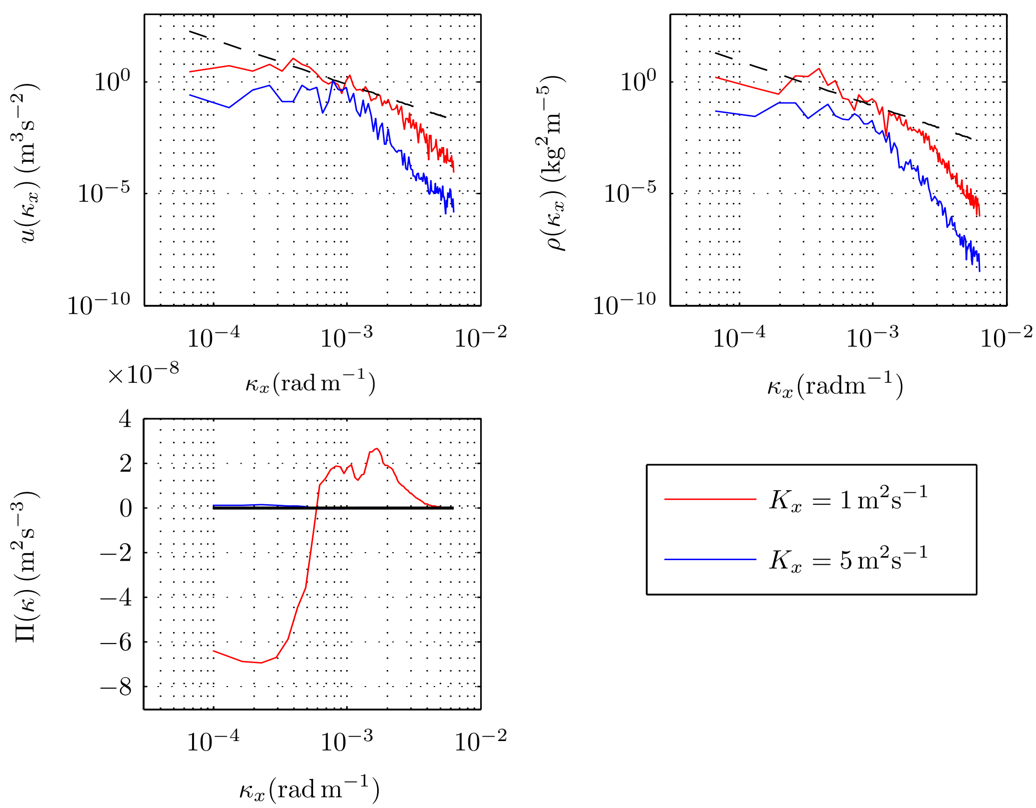

Figure 8: Similar to Fig. 7 but for an SGS model with constant lateral SGS viscosities and an analytically prescribed vertical SGS viscosity.

and Marshall, 1998). Vertical profiles of m, the ratio of the zonally and temporally averaged isopycnal slope, $-\langle b_y\rangle/\langle b_z\rangle$, to the slope along which fluid parcels exchange buoyancy in the $y-z$ plane, $\langle v'b'\rangle/\langle b'w'\rangle$, illustrate how efficiently the APE is converted to kinetic energy (Fig. 9). The variables b_y and b_z denote the meridional and vertical buoyancy gradients, respectively. Maximum extraction of APE occurs when $m = 2$ (Haine and Marshall, 1998). In unforced simulations of a frontal system, Fox-Kemper et al. (2008) found

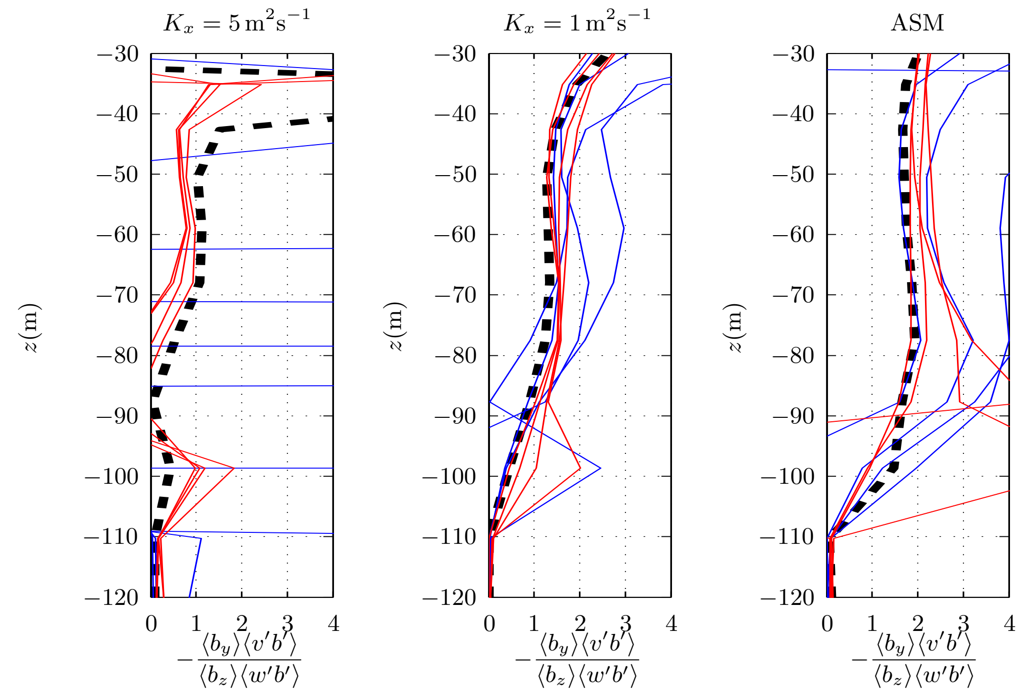

Figure 9: Vertical profiles of m, the ratio of the zonally averaged isopycnal slope, $-\langle b_y\rangle/\langle b_z\rangle$, to $\langle b'w'\rangle/\langle b'v'\rangle$, the slope along which fluid parcels exchange buoyancy in the y–z plane, at $t = 11T_f$ where $T_f = 2\pi/f_0 = 17.5$ hours is one inertial period. We have further averaged the profiles over one inertial period centered at $t = 11T_f$. The different curves are profiles at different meridional locations. For the most efficient extraction of APE, $m = 2$ (Haine and Marshall, 1998). The black, dashed line represents $y = 96$km, the initial location of the density front. The blue lines correspond to four meridional locations starting at $y = 97$ km and spaced 1 km apart, to the north of $y = y_f$. The red lines correspond to four similarly spaced locations but to the south of $y = y_f$.

m settles to a value between one and two after six to seven inertial periods (assuming a Coriolis parameter of 10^{-4} rad s^{-1}).

For the ASM, by $t = 11T_f$, m is starting to attain values close to 2 at depths between 30 m and 80 m near the front, implying the eddies there are extracting APE efficiently. For $K_x = 1$ m^{2}s^{-1} the extraction of APE has not yet reached peak efficiency over a comparable range of depths but does so after a couple more inertial periods (not shown). In contrast, for $K_x = 5$ $\mathrm{m^2s^{-1}}$ the conversion of APE to kinetic energy is much less efficient. We confirmed this is also borne out in horizontal and meridional section plots of density that show a delayed onset of ML instabilities and frontal slumping when $K_x = 5$ $\mathrm{m^2s^{-1}}$, compared to $K_x = 1$ $\mathrm{m^2s^{-1}}$ and the ASM. The inability of the simulation with $K_x = 5$ $\mathrm{m^2s^{-1}}$ to extract APE efficiently is reflected in the weakened meandering of the front at later times (Fig. 3).

We found the efficiency with which the eddies extract APE changes with time and the runs with $K_x = 5$ $\mathrm{m^2s^{-1}}$ start to yield $m \approx 2$ at later times (after $18T_f$) but over smaller meridional and vertical distances when compared to $K_x = 1$ $\mathrm{m^2s^{-1}}$ and the ASM. We conclude excessively high K_x coupled with a background SGS vertical viscosity leads to inefficient conversion of APE to kinetic energy.

4.4. Eddy kinetic energy budget and SGS dissipation

This section examines the various terms in the eddy kinetic energy (EKE) budget and explores the balance between them. We average the terms temporally (over one inertial period), zonally and meridionally (near the front). We also relate, where possible, magnitudes of the dominant production term in the EKE budget to scaling estimates derived previously in the literature.

The non-dimensional EKE budget is given by,

$$\frac{\partial\left(u_i'u_i'\right)}{\partial t} = \underbrace{-u_j'\frac{\partial\left(u_i'u_i'+e_{\mathrm{sgs}}\right)}{\partial x_j} - \langle\tilde{u}_j\rangle\frac{\partial\left(u_i'u_i'+e_{\mathrm{sgs}}\right)}{\partial x_j}}_{\text{Advection}} \underbrace{-\left(u_i'u_j'\right)\left[\left.\frac{\partial\tilde{u}_i}{\partial x_j}\right|_{\mathrm{geo}} + \left.\frac{\partial\tilde{u}_i}{\partial x_j}\right|_{\mathrm{ageo}}\right]}_{\text{Shear production}}$$
$$+ \underbrace{b'w'}_{\text{Buoyancy}} \underbrace{-\frac{1}{\rho_0}\frac{\partial\left(p'u_i'\right)}{\partial x_i}}_{\text{Pressure transport}} + \underbrace{\tau_{ij}^d\tilde{s}_{ij}}_{\text{SGS dissipation }(\epsilon_{\mathrm{sgs}})}, \tag{13}$$

where the angled brackets denote zonal averaging and the primed variables are fluctuations from the corresponding zonal averages. For instance, u_i' is the deviation of $\tilde{u}_i$ from its zonal average, $\langle\tilde{u}_i\rangle$. The terms in (13) describe the different gain and loss terms that produce (or destroy) the kinetic energy of eddies spanning the entire range of scales resolved in our simulation. Both the resolved-scale and SGS kinetic energy contribute to the advection term but our plots do not show the subgrid contribution as we lack a parameterization for e_{sgs}.

Anisotropic Smagorinsky Model. The near-surface resolved-scale eddy kinetic energy (EKE) budget (Fig. 10, left panel) shows $\epsilon_{\mathrm{sgs}} \sim \mathrm{O}(10^{-6})$ m^{2}s^{-3} and is balanced approximately by ageostrophic shear production. The other terms in the budget are much smaller in comparison. Monin-Obukhov (MO) theory prescribes the relevant scaling parameters within the inertial surface-layer, namely, u_* for velocity and z for the vertical length scale. Thus, estimating $\epsilon_{\mathrm{sgs}} \sim u_*^3/z$, where $u_* = 0.01$ ms^{-1} is the friction velocity (corresponding to $\tau_x = 0.1$ Nm^{-2}) and $z \sim O(1)$ m we obtain $\epsilon_{\mathrm{sgs}} \sim O(10^{-6})$ m^{2}s^{-3}, which is in reasonable agreement with the near-surface values. Although we have used the MO variables u_* and z to scale the dominant production terms, this near-surface layer is slightly different from the traditional MO layer be-

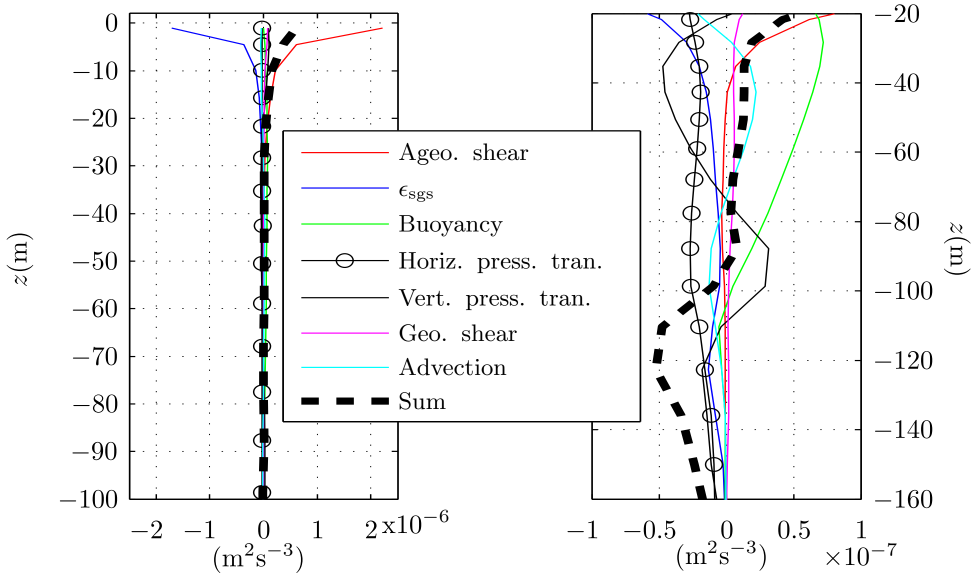

Figure 10: Left: EKE budget with zonal, meridional (near the front) and temporal (over one inertial period) averaging, obtained using the ASM, for $-100\text{m} < \text{z} < 0\text{m}$ at $t = 15T_f$, where $T_f = 2\pi/f_0 = 17.5$ hours is one inertial period. Right: the budget terms for $-160\text{m} < \text{z} < -20\text{m}$. The zonal averaging is done along an E-W section at $y = 96$ km. The meridional averaging is performed near the front, over a distance across which the magnitude of the zonally-averaged lateral density gradient decreases by less than 10% (Fox-Kemper et al., 2008). The range on the x-axis is different in the two plots. The circles on the lateral pressure transport profile indicate the vertical grid levels.

cause the imposed surface buoyancy flux is zero, which should theoretically yield an infinitely deep MO layer. The finiteness in depth of this MO-like layer, even in the absence of surface buoyancy fluxes is due to Ekman advection by downfront winds (discussed later).

Deeper down in the ML ($-100\text{m} < z < -20\text{m}$), the EKE budget exhibits a more complex balance involving multiple terms (Fig. 10, right panel). The dominant source term is the vertical buoyancy flux, $\langle b'w' \rangle$, whose positive sign is consistent with the notion of submesoscale eddies restratifying the flow by converting APE to kinetic energy (Fox-Kemper et al., 2008). The vertical buoyancy flux is balanced mostly by a combination of pressure transport and SGS dissipation. The pressure transport terms are larger in magnitude than the SGS dissipation at most depths and change sign within the ML. For instance, the sign of the vertical pressure transport implies, in a zonally-averaged sense, the transport of EKE generated within $-70\text{m} < \text{z} < -20\text{m}$ downwards to $-110\text{m} < \text{z} < -70\text{m}$. There is some advection of EKE due to vertical velocity fluctuations although it plays a relatively minor role. In summary, the source terms in the resolved-scale EKE budget are offset primarily by a combination of subgrid dissipation, which dissipates the EKE locally, and pressure transport, which transfers the EKE to other regions.

We now attempt to justify the magnitude of the dominant production term at depths $-100\text{m} < z < -20\text{m}$. Mahadevan et al. (2010) introduced a non-dimensional parameter, $r \equiv \left|\psi/\psi_e\right| = \tau_x/(0.06\rho H^2\langle b_y\rangle)|_{t=0}$, where ψ is the overturning stream function, ψ_e is the eddy stream function, H is the MLD and $b_y = \partial b/\partial y$ is the meridional buoyancy gradient. The overturning stream function is defined as, $\psi = -\int_0^z \langle V\rangle\, dz = \int_0^y \langle W\rangle\, dy$, where V and W denote dimensional meridional and vertical velocities, respectively. The eddy stream function is defined as follows:

$$\psi_e = \alpha\left(\frac{\alpha\langle v'b'\rangle\langle b_z\rangle - \alpha^{-1}\langle w'b'\rangle\langle b_y\rangle}{\langle b_y\rangle^2 + \alpha^2\langle b_z\rangle^2}\right), \quad \alpha \ll 1. \tag{14}$$

We choose $\alpha = 10^{-3}$ following Mahadevan et al. (2010), who found Eq. 14 is insensitive to α over a range 10^{-2}–10^{-4}. The angled brackets $\langle\rangle$ denote zonal averaging. The parameter r is an indicator of the competition between de-stratification induced by down-front winds and restratification by the mixed layer eddies. High values of r imply the down-front winds are strong enough to prevent a net relaxation of the front by the mixed layer eddies. Low values imply downfront winds too weak to prevent net restratification by the ML eddies. For r close to unity, presumably, the two tendencies balance each other resulting in an equilibrium. Using the initial values of H and b_y, we estimate $r = 1.6$. Comparing the peak magnitudes of ψ and ψ_e (Fig. 11) shows they are approximately equal. Under such quasi-equilibrium conditions, theory predicts the sum of the buoyancy flux and the geostrophic shear scales with the "Ekman buoyancy flux," or EBF (Thomas and Taylor, 2010), given by:

$$\mathrm{EBF} = \frac{\tau_x}{\rho_0 f_0} \langle \left| S^2 \right| \rangle, \tag{15}$$

where $S^2 = -b_y$. Thomas and Taylor (2010) held S^2 constant in the cross-front direction thereby maintaining a reservoir of constant APE. Here, S^2 and the APE vary with time as we do not restore the buoyancy gradient in the S-N direction.

Substituting $\tau_x = 0.1$ Nm^{-2} and $\langle \left| S^2 \right| \rangle = 0.6 \times 10^{-7}$ s^{-2} (Fig. 12) in (15) we obtain EBF $= 0.58 \times 10^{-7}$ m^{2}s^{-3}.

The geostrophic shear production is much smaller than the buoyancy flux at mid-ML depths and the latter scales with the EBF for depths between 20 m, and 70 m (Fig. 10, right panel). Thus, for the present value of $r = 1.6$, the magnitude of the dominant production term in the EKE budget obtained using the ASM is consistent with the scaling put forth by Thomas and Taylor (2010). For values of r significantly greater or smaller than unity, such a scaling might not be valid. From the low magnitude of the residual (thick dashed line) for $-70\text{m} < \text{z} < -20\text{m}$ we infer the sum of the pressure transport terms and the SGS dissipation also scales on the EBF. The relative

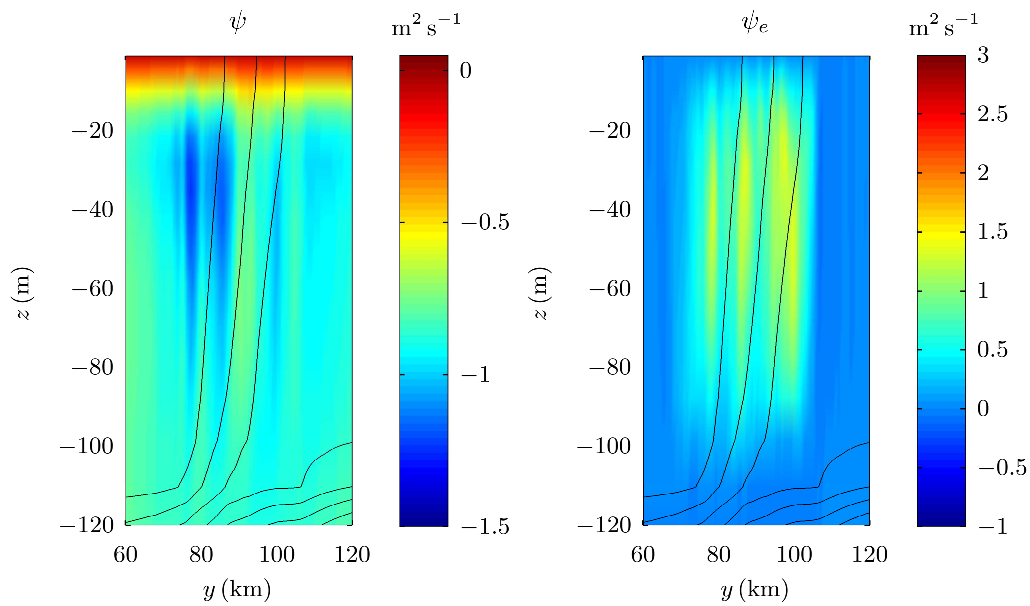

Figure 11: ASM. Vertical sections of the overturning stream function, ψ, and the eddy stream function, ψ_e, after $t = 15T_f$, where $T_f = 2\pi/f_0 = 17.5$ hours is one inertial period. Solid lines are isopycnals.

proportions of EKE destroyed locally by the subgrid model and radiated away by pressure transport depend on the subgrid constant. Increasing the subgrid constant enhances the fraction of EKE destroyed locally while decreasing the same causes more of the EKE to be radiated away.

Figure 10 suggests there is a depth that separates the ML into two regions, one where the EKE balance can be described by MO-scaling (in terms of u_* and z) and the other where submesoscale dynamics enters the EKE balance directly. To estimate this depth we compute an effective MO length scale, $L_{\mathrm{MO,eff}}$, by modifying the definition for the MO length and replacing the buoyancy flux in the numerator with the EBF. This length scale is similar to the MO length scale to the extent it determines whether the EKE budget is

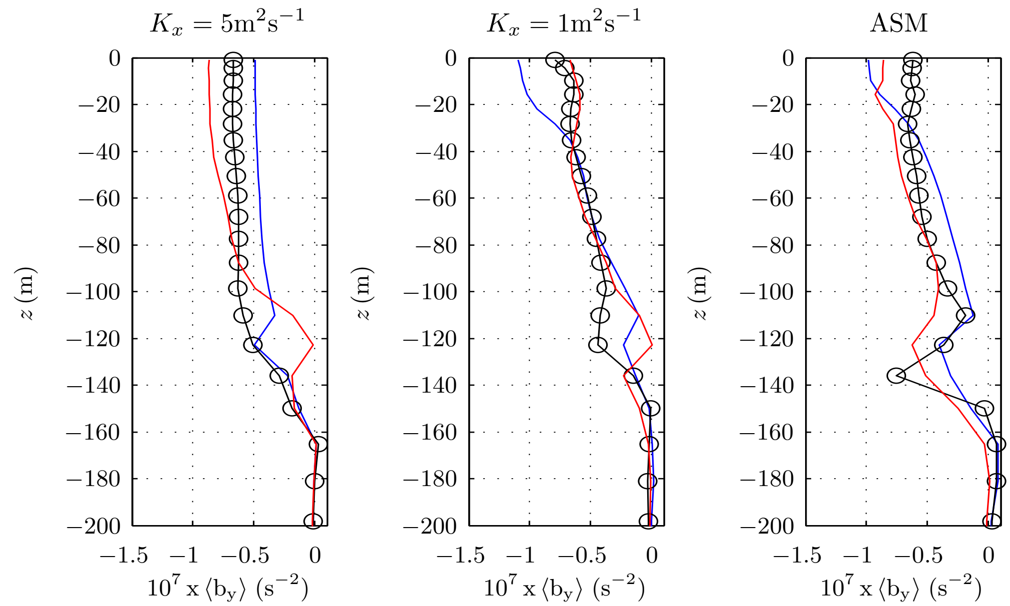

Figure 12: Vertical profiles of zonally averaged $10^7 \times \langle b_y \rangle$ (s^{-2}) at $y = 96$km and $t = 15T_f$, where $T_f = 2\pi/f_0 = 17.5$ hours is one inertial period. We further average the profiles over one inertial period centered at $t = 15T_f$. The profiles are shown at three meridional locations: (i) $y = y_f$ (black); (ii) $y = y_f - 2.5$ (red); and (iii) $y = y_f + 2.5$ (blue), where $y = y_f$ (in km) denotes the initial meridional location of the front. The circles on the black curve denote the vertical grid levels.

dominated by shear (ageostrophic shear) or buoyancy (due to restratification by eddies). For the magnitudes of τ_x and $\langle S^2 \rangle$ considered here, $\langle S^2 \rangle$—through the EBF—sets the depth of the layer in which the dominant terms in the EKE budget obey MO scaling; it does not influence explicitly the magnitudes of these terms within this layer as they can be explained using the MO variables u_* and z. The situation is different in the region below the MO-like layer where the EKE budget is dominated by the buoyancy flux, whose magnitude depends explicitly on $\langle S^2 \rangle$, as discussed above. Scaling the ageostrophic

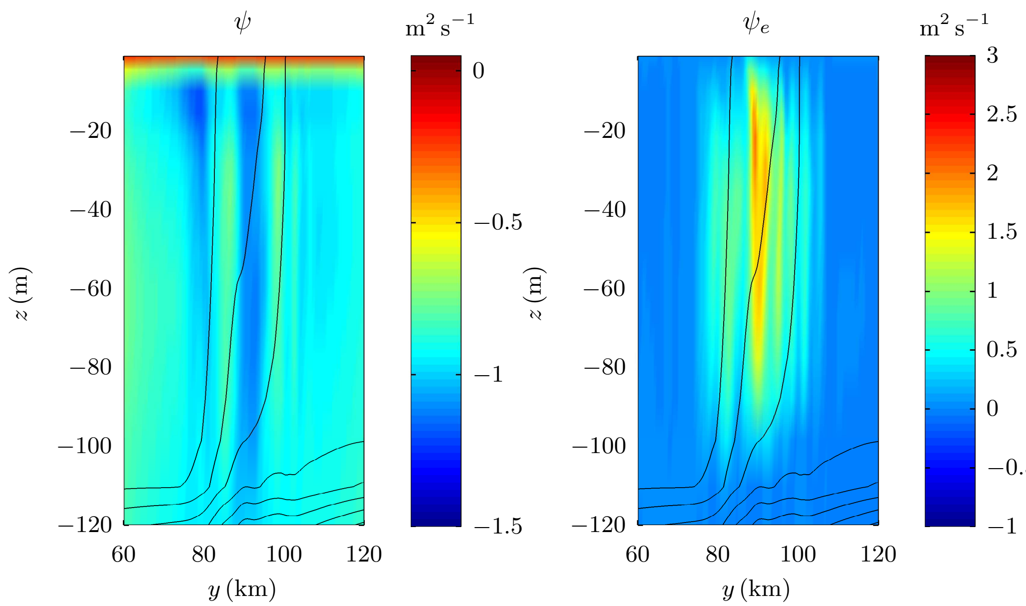

Figure 13: $K_x = 1\mathrm{m}^2\mathrm{s}^{-1}$. Vertical sections of the overturning stream function, ψ, and the eddy stream function, ψ_e, after $t = 15T_f$, where $T_f = 2\pi/f_0 = 17.5$ hours is one inertial period. Solid lines are isopycnals.

shear production term near the surface as u_*^3/z (from MO scaling), we obtain $L_{\mathrm{MO,eff}} \sim u_*^3/\mathrm{EBF}$. Substituting values for u_* and EBF, $L_{\mathrm{MO,eff}} = 17.2$ m which is consistent with our results (Fig. 10, left panel).

$\mathbf{K_x = 1\ m^2s^{-1}}$. Plots of ψ and ψ_e are qualitatively similar to Fig. 11 and show the stream functions attain their maximum values near the front. We focus on depths greater than 20 m where we found the differences in the EKE budget between the constant-K_x and the ASM simulations to be the greatest. When $K_x = 1\ \mathrm{m}^2\mathrm{s}^{-1}$ (Figs. 14, left panel) the nature of balance in the EKE budget differs considerably from that seen in Fig. 10. While the buoyancy flux remains the dominant term and scales with the EBF, it is balanced solely by pressure transport, the other terms playing a negligible role in the budget. Unlike ASM, the horizontal pressure transport is significantly larger than the vertical pressure transport. The low values of SGS dissipation show the background vertical SGS viscosity and the constant lateral SGS viscosity together are unable to produce significant local destruction of the kinetic energy, whereas recent experimental studies in the Kuroshio (D'Asaro et al., 2011) show significantly enhanced levels of dissipation near fronts. Low SGS dissipation leaves radiation of EKE as the only available option for the removal of kinetic energy, as evidenced by the presence of waves near the front (Fig. 4).

$\mathbf{K_x = 5\ m^2s^{-1}}$. The peak magnitude of ψ_e is lesser than that for $K_x = 1$ $\mathrm{m^2s^{-1}}$ and the ASM, which is consistent with the reduced conversion of APE to kinetic energy when $K_x = 5\mathrm{m^2s^{-1}}$. The dominant terms in the EKE budget (Fig. 14) scale as $O(10^{-8})$ $\mathrm{m^3s^{-2}}$, an order of magnitude smaller than what we expect from the arguments outlined before. The drastically reduced buoyancy flux implies weaker restratification compared to the ASM and $K_x = 1$ $\mathrm{m^2s^{-1}}$. The weaker restratification is a direct consequence of the inefficient conversion of APE to kinetic energy (Fig. 9). While the maximum zonally-averaged buoyancy flux within the mixed layer increases with time, $\langle b'w' \rangle$ starts to scale on the EBF only after t = 20–21T_f. Even so, the maximum $\langle b'w' \rangle$ is smaller than the corresponding values for the ASM and $K_x = 1$ $\mathrm{m^2s^{-1}}$ by a factor of two or more.

The above discussion on the EKE budgets for constant K_x assumes a background vertical SGS viscosity. For the ASM, we confirmed ϵ_{sgs} is determined primarily by vertical gradients of velocity with the lateral gradients

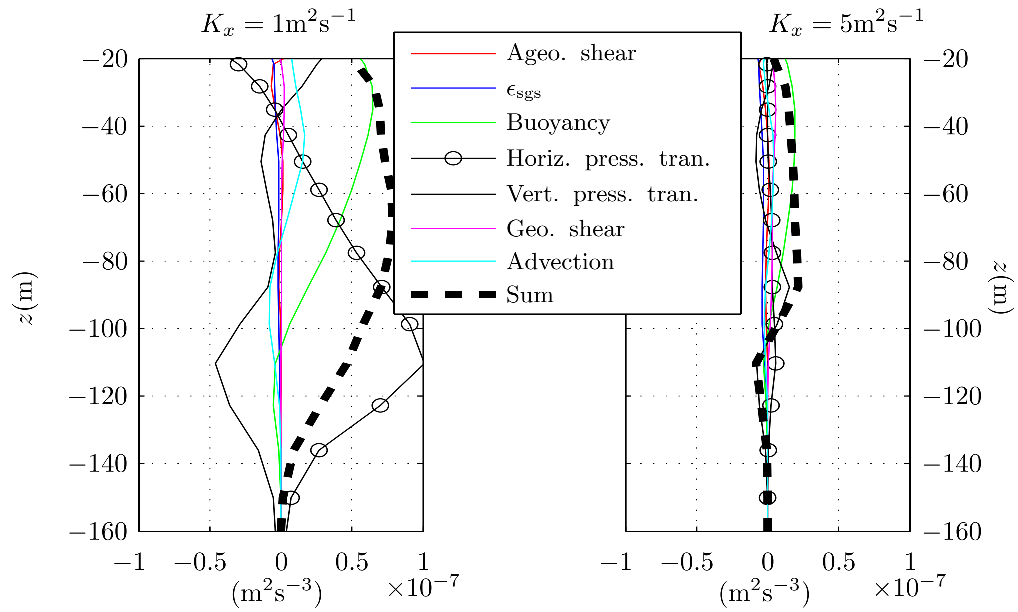

Figure 14: EKE budget with zonal, meridional (near the front) and temporal (over one inertial period) averaging for $-160\mathrm{m} < \mathrm{z} < -20\mathrm{m}$ at $t = 15T_f$, where $T_f = 2\pi/f_0 = 17.5$ hours is one inertial period. Left: $K_x = 1$ $\mathrm{m}^2\mathrm{s}^{-1}$, Right: $K_x = 5$ $\mathrm{m}^2\mathrm{s}^{-1}$. The zonal averaging is done along an E-W section at $y = 96$ km. The meridional averaging is performed near the front, over a distance across which the magnitude of the zonally-averaged lateral density gradient decreases by less than 10% (Fox-Kemper et al., 2008). The circles on the black curves denote the vertical grid levels.

of the same playing a secondary role. Thus, we attribute the low levels of SGS dissipation in the constant K_x simulations to the use of a background vertical SGS viscosity that does not take into account the vertical shear of horizontal velocity. It follows increasing the value of K_x (or K_y) while using a background SGS viscosity will not lead to enhanced SGS dissipation.

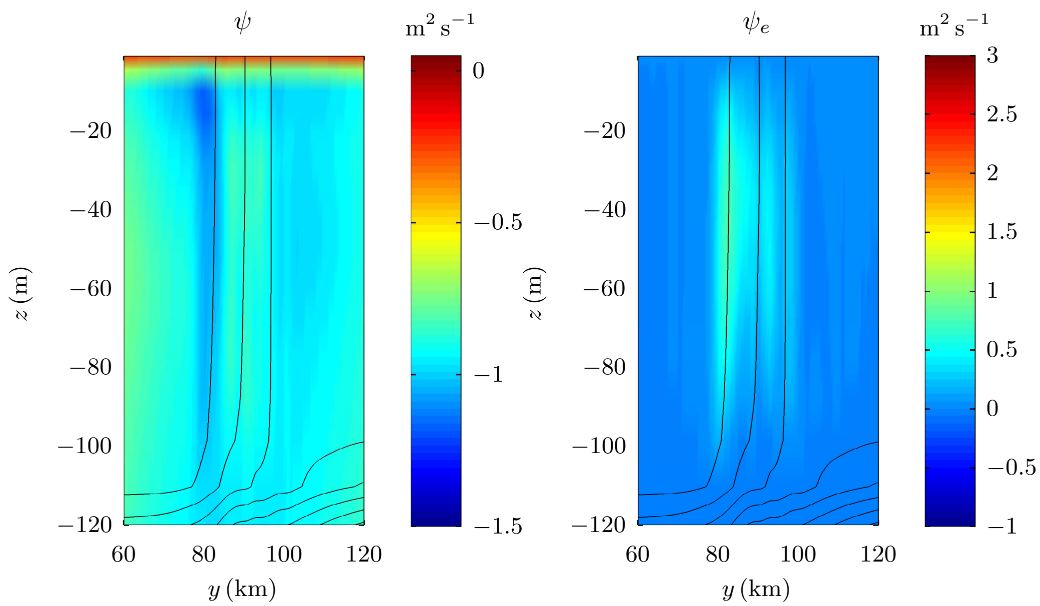

Figure 15: $K_x = 5\mathrm{m}^2\mathrm{s}^{-1}$. Vertical sections of the overturning stream function, ψ, and the eddy stream function, ψ_e, after $t = 15T_f$, where $T_f = 2\pi/f_0 = 17.5$ hours is one inertial period. The solid lines are isopycnals.

4.5. Evolution of $\left|\partial b/\partial y\right|$ *and* ϵ_{sgs}

To further explore the modification of the buoyancy gradient by the velocity field we plot the zonally averaged values of $\left|S^2\right|$ at a depth of 50 m, approximately half the depth of the ML. The reduction of $\left|\partial b/\partial y\right|$ in the vicinity of the front at $t = 15T_f$ (green curve) and $t = 11T_f$ (blue curve) for simulations with $K_x = 1\ \mathrm{m}^2\mathrm{s}^{-1}$ and the ASM, respectively, is due to the extraction of APE by the eddies, as discussed in Sec. 4.3. There is intensification of $\langle\left|S^2\right|\rangle$ at some meridional locations due to frontogenesis by the underlying strain field (Capet et al., 2008c). This is more pronounced with the ASM than in the other two cases. The amplification of the buoyancy gradient is weakest with $K_x = 5\ \mathrm{m}^2\mathrm{s}^{-1}$, as seen in the minimal distortion

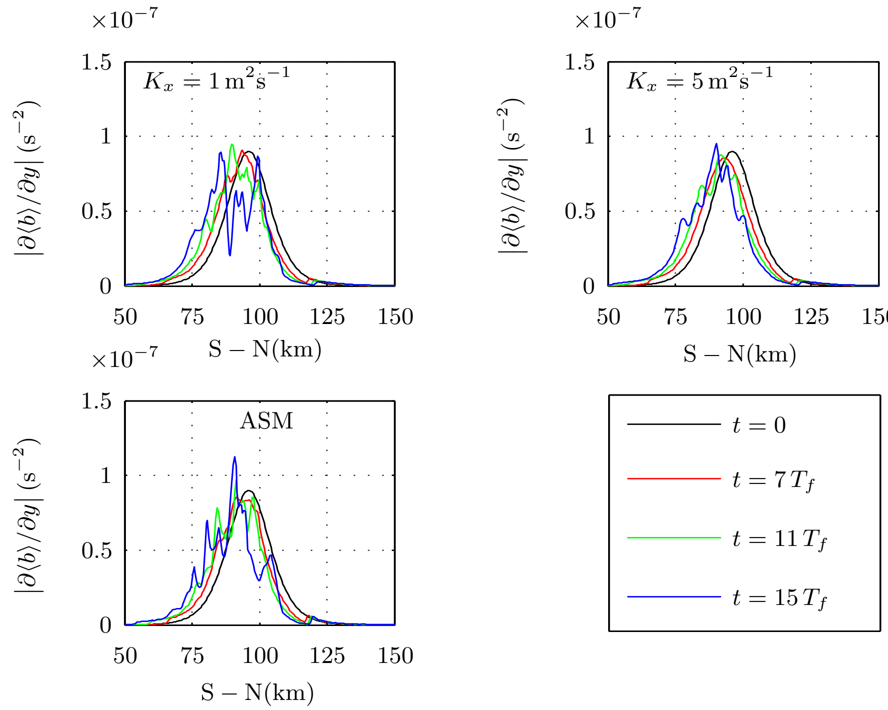

Figure 16: Snapshots of zonally-averaged $|\partial b/\partial y|$ at $z = -50$ m for $t = 0$, $t = 7T_f$, $t = 11T_f$ and $t = 15T_f$, where $T_f = 2\pi/f_0 = 17.5$ hours is one inertial period. The profiles are further averaged in time over one inertial period centered at the time of the snapshot.

of the initial $\langle|S^2|\rangle$ profile. A comparison of vertical profiles of $\mathbf{Q}.\nabla_h\rho$ near the front in Fig. 17, where $\mathbf{Q} = -\big(\partial_x u\partial_x\rho + \partial_x v\partial_y\rho,\, \partial_y u\partial_x\rho + \partial_y v\partial_y\rho\big)$ is the "Q-vector" (Sanders and Hoskins, 1990), confirms the frontogenesis is weakest for $K_x = 5$ m^{2}s^{-1}.

We conclude this section with time-depth plots of ϵ_{sgs}, N^2 and $|\partial b/\partial y|$ over the entire course of the simulation (Figs. 18—20) which make evident the differences in the temporal evolution of the flow for $K_x = 1$ m^{2}s^{-1}, $K_x = 5$ m^{2}s^{-1} and the ASM. We choose vertical profiles at the horizontal center of the domain, i.e., midway between the E-W and S-N boundaries, as

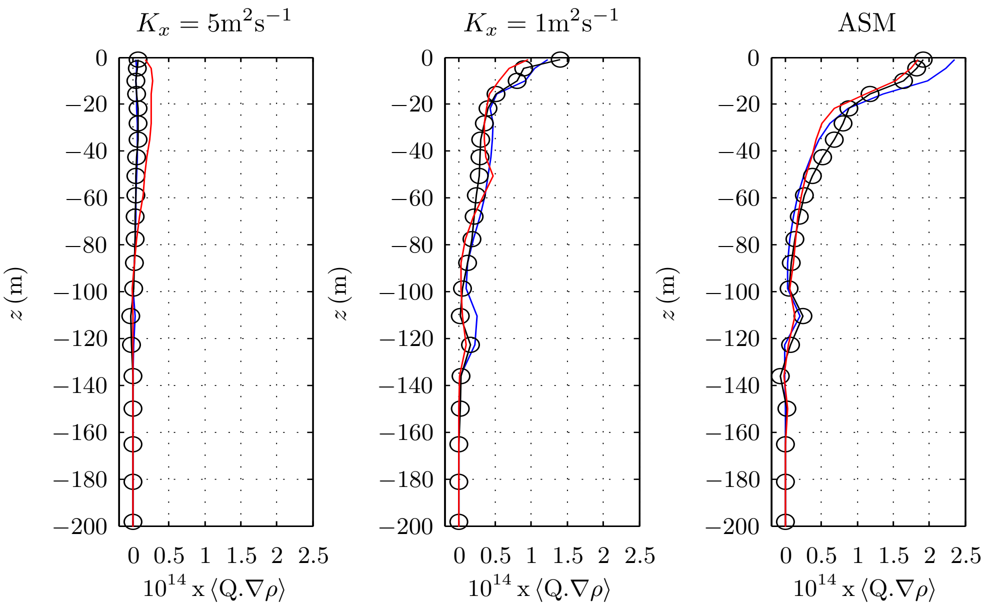

Figure 17: Vertical profiles of zonally averaged $10^{14} \times \mathbf{Q}.\nabla\rho$ ($\mathrm{kg}^2\mathrm{m}^{-8}\mathrm{s}^{-1}$), where $\mathbf{Q}$ is the "Q-vector." We further average the profiles over one inertial period centered at $t = 15T_f$, where $T_f = 2\pi/f_0 = 17.5$ hours is one inertial period. The profiles are shown at three meridional locations: (i) $y = y_f$ (black); (ii) $y = y_f - 2.5$ km (red); and (iii) $y = y_f + 2.5$ km (blue), where $y = y_f = 96$ km denotes the initial meridional location of the front. The circles on the black curve denote the vertical grid levels.

representative for this purpose.

The development of instabilities is slowest for $K_x = 5$ $\mathrm{m}^2\mathrm{s}^{-1}$ (Fig. 18), as seen in the evolution of ϵ_{sgs}, for instance, which begins to attain non-negligible values only after 9–10 inertial periods. This contrasts the plots for $K_x = 1$ $\mathrm{m}^2\mathrm{s}^{-1}$ and ASM, where we see the presence of regions within the ML with high ϵ_{SGS} after 5—6 inertial periods. The temporal evolution of N^2 shows restratification is weakest for $K_x = 5$ $\mathrm{m}^2\mathrm{s}^{-1}$, which, as we saw earlier, is the result of diminished buoyancy fluxes (Fig. 14) and inefficient conversion

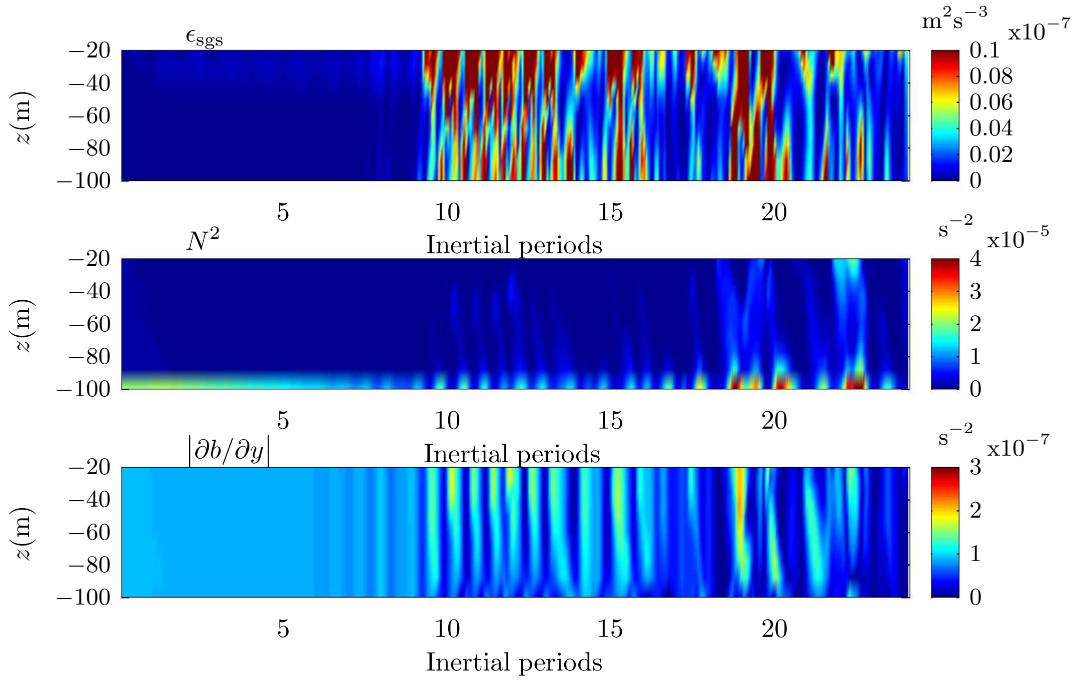

Figure 18: $K_x = 5$ m^{2}s^{-1}: A representative vertical section-plot showing the local time evolution of $\epsilon_{\rm sgs}$, N^2 and $\left|\partial b/\partial y\right|$ at a point midway between the E–W and S–N walls.

of APE to kinetic energy (Fig. 9). Relative to the initial peak value of $\left|S^2\right|$ ($\approx 10^{-7}$ s^{-2}), the amplification of $\left|S^2\right|$ is lesser for $K_x = 5$ m^{2}s^{-1} compared to $K_x = 1$ m^{2}s^{-1} and ASM. For the latter two cases, the local intensification of $\left|S^2\right|$ occurs at both shallow depths and deeper down in the ML, in some cases enhancing $\left|S^2\right|$ to three times its initial value (0.9×10^{-7} s^{-2}).

5. Summary

This study contrasts the performance of two subgrid closures in simulations of an oceanic density front forced by downfront winds. The simulated domains are large enough to contain mesoscale eddies and fine enough to re-

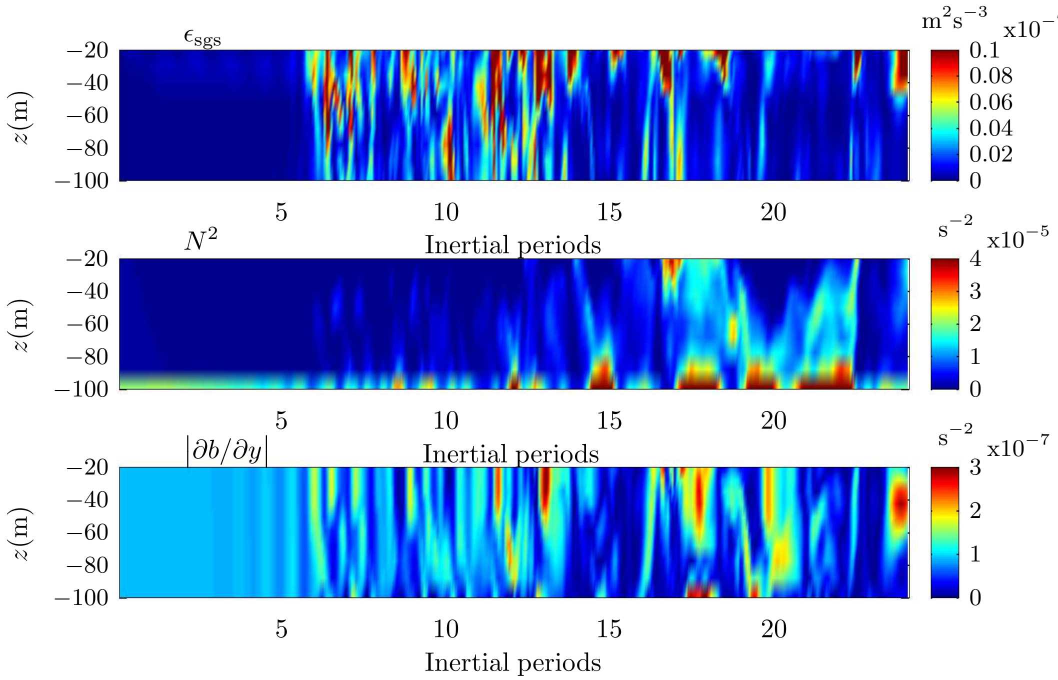

Figure 19: $K_x = 1$ m^{2}s^{-1}: A representative vertical section-plot showing the local time evolution of ϵ_{sgs}, N^2 and $|\partial b/\partial y|$ at a point midway between the E–W and S–N walls.

solve a part of the submesoscale spectrum. The two SGS closures we choose are: (i) constant lateral SGS viscosities and an analytically prescribed background vertical SGS viscosity; and (ii) an anisotropic version of the classical Smagorinsky model, developed specifically for computational grids where the horizontal resolution is much coarser than the vertical resolution (Roman et al., 2010). The Anisotropic Smagorinsky model (or ASM) prescribes both lateral and vertical SGS viscosities as functions of the resolved-scale strain rate.

Our simulations show the temporal and spatial evolution of the submesocale instabilities is sensitive to the underlying subgrid parameterization

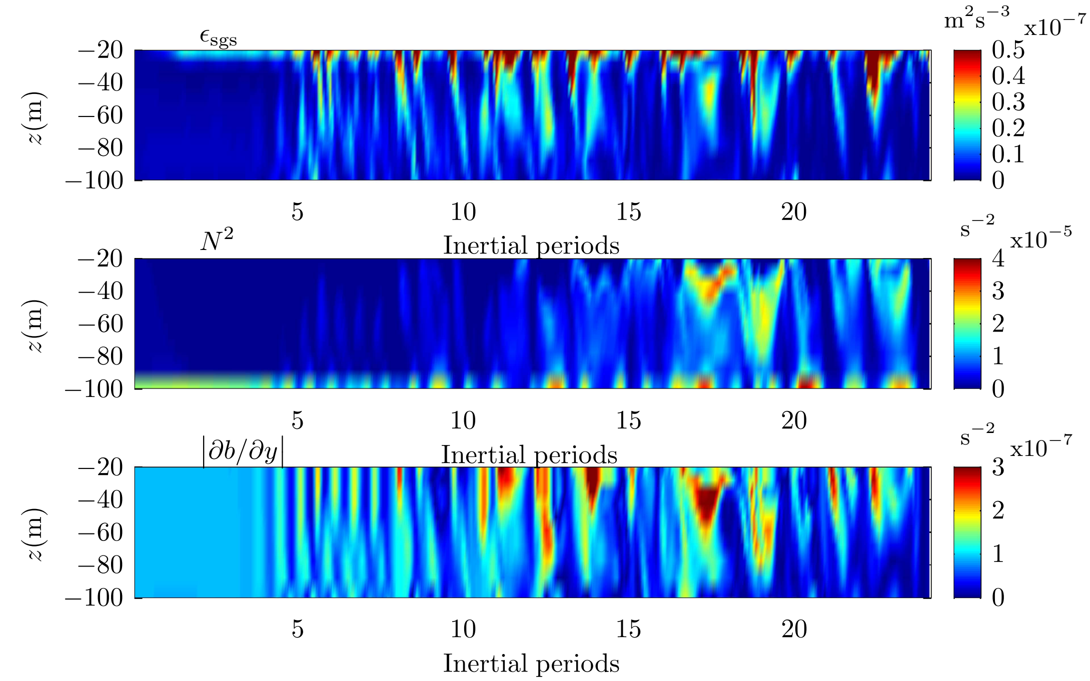

Figure 20: ASM: A representative vertical section-plot showing the local time evolution of $\epsilon_{\rm sgs}$, N^2 and $|\partial b/\partial y|$ at a point midway between the E–W and S–N walls. The range on the $\epsilon_{\rm sgs}$ colour bar differs from those in Figs. 18—19.

which, we find, can influence the dynamics at scales far removed from the grid cutoff scale. In particular, the following exhibit strong dependence on both the choice of the SGS model and the model constant for a given SGS model: (i) the strength of the inverse and forward cascades; (ii) the efficiency of conversion of APE to kinetic energy; (iii) strength of frontogenesis; and (iv) the resolved-scale EKE budgets.

Both $K_x = 1$ m^{2}s^{-1} and the ASM predict an inverse cascade at the large scales and the onset of a forward cascade at O(10 km) scales. For the ASM, the peak magnitude of the inverse cascade decreases upon increasing the SGS model constants. The simulations for $K_x = 5\ \mathrm{m^2s^{-1}}$ fare the worst as they yield strongly diminished inverse and forward cascades.

For $K_x = 1\ \mathrm{m^2s^{-1}}$ and the ASM, the conversion of APE to kinetic energy is more efficient than for $K_x = 5\ \mathrm{m^2s^{-1}}$. In the former two cases, the flow is able to extract APE with the maximum theoretical efficiency over a much greater range of depths within the ML, when compared to $K_x = 5\ \mathrm{m^2s^{-1}}$. The weaker inverse cascade for $K_x = 5\ \mathrm{m^2s^{-1}}$ is a direct consequence of the inability of the flow to utilize the APE efficiently.

The simulations with $K_x = 5\ \mathrm{m^2s^{-1}}$ yield negligible frontogenesis compared to $K_x = 1\ \mathrm{m^2s^{-1}}$ and the ASM, as measured by the magnitude of $\mathbf{Q}.\nabla\rho$, which implies lesser intensification of the buoyancy gradient by the strain field.

The resolved-scale EKE budgets in all the simulations are qualitatively similar near the surface within a MO-like layer where the balance is primariliy between ageostrophic shear and SGS dissipation. The lateral buoyancy gradient sets the depth of the MO-like layer but does not directly determine the magnitudes of the dominant terms in the budget within this layer, which are found to scale with the MO variables u_* and z. Below the MO-like layer the EKE budgets obtained using the ASM, $K_x = 1\ \mathrm{m^2s^{-1}}$ and $K_x = 5\ \mathrm{m^2s^{-1}}$ are all significantly different from each other. The dominant production term in all three cases is the buoyancy flux, which is positive, indicating restratification by the ML instabilities. The differences arise in: (i) the magnitude of the buoyancy flux; and (ii) how the buoyancy flux is balanced in the EKE budget.

For $K_x = 1\ \mathrm{m^2s^{-1}}$ and the ASM, the magnitude of the buoyancy flux is consistent with existing scaling arguments in the literature (Thomas and Taylor, 2010), which is not the case for $K_x = 5\ \mathrm{m^2s^{-1}}$ where the corresponding values are an order of magnitude smaller. Indeed, this is true of all the terms in the EKE budget for $K_x = 5\ \mathrm{m^2s^{-1}}$.

The buoyancy flux, for the ASM, is balanced by a combination of pressure transport and SGS destruction implying the EKE can either be destroyed locally (through SGS destruction) or transported away (by pressure transport). This is consistent with recent experiments which show enhanced destruction near fronts (D'Asaro et al., 2011). In the simulations with constant K_x, however, the buoyancy flux is balanced entirely by pressure transport with negligible SGS destruction, which sugests insufficient dissipation by the SGS model.

We emphasize the weak SGS dissipation in the constant K_x simulations is a consequence of using a background SGS vertical viscosity, and not of the value of K_x. A better parameterization for the vertical SGS viscosity coupled with constant lateral SGS viscosities will likely yield more realisic EKE budgets with sufficient SGS dissipation though it is unclear whether this will also reduce the sensitivity of the results to K_x.

We conclude the parameterization of subgrid diffusion can have important consequences for the evolution of submesoscale instabilities in a frontal system forced by downfront winds. Using a constant value for the lateral SGS viscosity, K_x, is the simplest option but can lead to unreliable results. In particular, we find the simulation results can be quite sensitive to K_x when used in conjunction with an analytically prescribed background vertical SGS viscosity, K_v. Too high a value for K_x leads to weak inverse and forward cascades, inefficient extraction of APE, strongly reduced frontogenesis and an EKE budget whose dominant production term, the buoyancy flux, scales incorrectly. On the other hand, too low a value predicts a quicker evolution of the instabilities and more realistic buoyancy fluxes but relies completely on pressure transport to remove the EKE, which is inconsistent with recent experiments. The EKE budgets predicted by the ASM are closer to reality. If, however, one wishes to use a constant lateral SGS viscosity, it might be worth exploring the use of more sophisticated one-dimensional SGS vertical mixing schemes in lieu of a background SGS vertical viscosity.

5.1. Acknowledgements

The authors acknowledge support from the National Science Foundation (NSF-OCE 0928138) and the Office of Naval Research (ONR N00014-09-1-0196, ONR N00014-12-1-0101). We thank Drs. Louis Goodman and Leif Thomas for useful comments and insights. For the simulations, we used IBM machines provided by Dr. Gaurav Khanna at the University of Massachusetts, Dartmouth (NSF, PHY-0902026).

References

Boccaletti, G., Ferrari, R., Fox-Kemper, B., 2007. Mixed layer instabilities and restratification . Journal of Physical Oceanography 37, 2228–2250.

Brasseur, J.G., Wei, T., 2010. Designing large-eddy simulation of the turbulent boundary layer to capture law-of-the-wall scaling. Phys. Fluids. 22, 1–21.

Capet, X., McWilliams, J.C., Molemaker, M.J., Shchepetkin, A.F., 2008a. Mesoscale to submesoscale transition in the California Current System. Part II: Frontal processes . Journal of Physical Oceanography 38, 44–64.

Capet, X., McWilliams, J.C., Molemaker, M.J., Shchepetkin, A.F., 2008b. Mesoscale to submesoscale transition in the California Current System. Part III: Energy balance and flux . Journal of Physical Oceanography 38, 2256–2269.

Capet, X., McWilliams, J.C., Molemaker, M.J., Shchepetkin, A.F., 2008c. Mesoscale to submesoscale transition in the California Current System. Part I: Flow structure, eddy flux and observational tests . Journal of Physical Oceanography 38, 29–43.

Charney, J.G., 1971. Geostrophic turbulence . J. Atmos. Sci. 28, 1087–1095.

D'Asaro, E., Lee, C., Rainville, L., Harcourt, R., Thomas, L., 2011. Anisotropy and coherent structures in planetary turbulence . Science 332, 318–322.

Fox-Kemper, B., Ferrari, R., 2008. Parameterization of mixed layer eddies. Part II: Prognosis and impact. Journal of Physical Oceanography 38, 1166–1179.

Fox-Kemper, B., Ferrari, R., Hallberg, R.W., 2008. Parameterization of mixed layer eddies. Part I: Theory and diagnosis. Journal of Physical Oceanography 38, 1145–1165.

Fox-Kemper, B., Menemenlis, D., 2008. Can large-eddy simulation techniques improve mesoscale-rich ocean models?, in: Hecht, M., Hasume, H.

(Eds.), Ocean Modeling in an Eddying Regime, Geophysical Monograph 177, American Geophysical Union. pp. 319–338.

Germano, M., Piomelli, U., Moin, P., Cabot, W.H., 1991. A dynamic subgrid-scale eddy viscosity model. Phys. Fluids. 3, 1760–1765.

Haine, T.W.N., Marshall, J., 1998. Gravitational, symmetric and baroclinic instability of the ocean mixed layer . Journal of Physical Oceanography 28, 634–658.

Harcourt, R.R., D'Asaro, E.A., 2008. Large-eddy simulation of langmuir turbulence in pure wind seas. Journal of Physical Oceanography 38, 1542–1562.

Kamenkovich, V.M., 1977. Fundamentals of Ocean Dynamics. Elsevier, pp. 408.

Klein, P., Hua, B.L., Lapeyre, G., Capet, X., Gentil, S.L., Sasaki, H., 2008. Upper ocean turbulence from high-resolution 3D simulations . Journal of Physical Oceanography 38, 1748–1763.

Large, W., McWilliams, J., Doney, S., 1994. Oceanic vertical mixing: A review and a model with a nonlocal boundary layer parameterization. Reviews of Geophysics 32, 363–403.

Lévi, M., Klein, P., Treguier, A.M., 2001. Impacts of sub-mesoscale physics on production and subduction of phytoplankton in an oligotrophic regime. Journal of Marine Research 59, 535–565.

Lilly, D.K., 1967. The representation of small-scale turbulence in numerical experiments, in: Proc. IBM Scientific Computing Symp. on Environmental Sciences, Thomas J. Watson Research Center, IBM, Yorktown Heights, NY. pp. 195–210.

Lilly, D.K., 1992. A proposed modification of the Germano subgrid scale closure method . Phys. Fluids 4, 633–635.

Mahadevan, A., 1996. A non-hydrostatic mesoscale ocean model. 1: Well-posedness and scaling. . Journal of Physical Oceanography 26, 1168–1880.

Mahadevan, A., 2006. Modeling vertical motion at ocean fronts. Ocean Modeling 14, 222–240.

Mahadevan, A., Archer, D., 2000. Modeling the impact of fronts and mesoscale circulation on the nutrient supply and biogeochemistry of the upper ocean. Journal of Geophysical Research 105, 1209–1225.

Mahadevan, A., Tandon, A., 2006. An analysis of mechanisms for submesoscale vertical motion at ocean fronts. Ocean Modeling 14, 241–256.

Mahadevan, A., Tandon, A., Ferrari, R., 2010. Rapid changes in mixed layer stratification driven by submesoscale instabilities and winds . Geophys. Res. Lett. 115, 1–12.

Marchesiello, P., Capet, X., Menkes, C., Kennan, S.C., 2011. Submesoscale dynamics in tropical instability waves. Ocean Modelling 39, 31–46.

McWilliams, J.C., 2003. Diagnostic force balance and its limits, in: Nonlinear

Processes in Geophysical Fluid Dynamics, Kluwer Academic Publishers. pp. 287–304.

McWilliams, J.C., Weiss, J.B., Yavneh, I., 1994. Anisotropy and coherent structures in planetary turbulence . Science 264, 410–413.

Miles, J., 1994. On transversely isotropic eddy viscosity. Journal of Physical Oceanography 24, 1077–1079.

Miles, J.W., 1961. On the stability of heterogeneous shear flows. J Fluid Mech 10, 496–508.

Moeng, C.H., Wyngaard, J.C., 1988. Spectral analysis of large eddy simulations of the convective boundary layer. J Atmos Sci 45, 3573–3587.

Molemaker, M.J., McWilliams, J.C., 2005. Baroclinic instability and loss of balance . J. Phys. Oceanogr. 35, 1505–1517.

Molemaker, M.J., McWilliams, J.C., Capet, X., 2010. Balanced and unbalanced routes to dissipation in an equilibriated Eady flow . J. Fluid Mech. 654, 35–63.

Ohya, Y., Nakamura, R., Uchida, T., 2008. Intermittent bursting of turbulence in a stable boundary layer with low-level jet. Boundary-Layer Meteorol 126, 349–363.

Ozgokmen, T., Iliescu, T., Fischer, P.F., 2009. Reynolds number dependence of mixing in a lock-exchange system from direct numerical and large eddy simulations. Ocean Modeling 30, 190–206.

Ozgokmen, T., Iliescu, T., Fischer, P.F., Srinivasan, A., Duan, J., 2007. Large eddy simulation of stratified mixing in two-dimensional dam-break problem in a rectangular enclosed domain. Ocean Modeling 16, 106–140.

Ozgokmen, T., Poje, A.C., Fischer, P.F., Haza, A.C., 2011. Large-eddy simulations of mixed layer instabilities and sampling strategies. Ocean Modeling 39, 311–331.

Pedlosky, J., 1987. Geophysical Fluid Dynamics. Springer, Berlin. 2nd edition.

Piomelli, U., Cabot, W.H., Moin, P., Lee, S., 1991. Subgrid-scale backscatter in turbulent and transitional flows. Phys. Fluids. 3, 1766–1771.

Roman, F., Stipcich, G., Armenio, V., Inghilesi, R., Corsini, S., 2010. Large eddy simulation of mixing in coastal areas. International Journal of Heat and Fluid Flow 31, 327–341.

Sanders, F., Hoskins, B.J., 1990. An easy method for estimation of Q-vectors from weather maps . Weather and Forecasting 5, 346–353.

Scotti, A., Meneveau, C., 1993. Generalized Smagorinsky model for anisotropic grids. Physics of Fluids 5, 2306–2308.

Scotti, A., Meneveau, C., Fatica, M., 1997. Dynamic Smagorinsky model on anisotropic grids . Physics of Fluids 9, 1856–1858.

Skyllingstad, E.D., Samelson, R.M., 2011. Baroclinic frontal instabilities and turbulent mixing in the surface boundary layer. Part I: Unforced . *submitted to* J. Phys. Oceanogr. .

Smagorinsky, J., 1963. General Circulation experiments with the primitive equations I. The basic experiment. Mon Weather Rev 91, 99–164.

Sullivan, P.P., Horst, T.W., Lenschow, D.H., Moeng, C., Weil, J.C., 2003. Structure of subfilter-scale fluxes in the atmospheric surface layer with application to large-eddy simulation modelling. J Fluid Mech 482, 101–139.

Sullivan, P.P., Mcwilliams, J.C., Melville, W.K., 2007. Surface gravity wave effects in the oceanic boundary layer: large-eddy simulation with vortex force and stochastic breakers. J Fluid Mech 593, 405–452.

Tandon, A., Garrett, C., 1994. Mixed layer restratification due to a horizontal density gradient . Journal of Physical Oceanography 24, 1419–1424.

Taylor, J.R., Ferrari, R., 2009. On the equilibriation of a symmetrically unstable front via a secondary shear instability . Journal of Fluid Mechanics 622, 103–113.

Taylor, J.R., Ferrari, R., 2010. Buoyancy and wind-driven convection at mixed layer density fronts . Journal of Physical Oceanography 40, 1222–1242.

Tejada-Martínez, A.E., 2009. A hybrid spectral/finite-difference large-eddy simulator of turbulent processes in the upper ocean. Ocean Modelling 30, 115–142.

Tennekes, H., Lumley, J.L., 1972. A First Course in Turbulence. The MIT Press, pp. 300.

Thomas, L., 2005. Destruction of potential vorticity by winds . Journal of Physical Oceanography 35, 2457–2466.

Thomas, L., Tandon, A., Mahadevan, A., 2007. Submesoscale ocean processes and dynamics, in: Hecht, M., Hasume, H. (Eds.), Ocean Modeling in an Eddying Regime, Geophysical Monograph 177, American Geophysical Union. pp. 217–228.

Thomas, L.N., Taylor, J.R., 2010. Reduction of the usable wind-work on the general circulation by forced symmetric instability . Geophysical Research Letters 37, 1–5.

Wajsowicz, R.C., 1993. A consistent formulation of the anisotropic stress tensor for use in models of the large-scale ocean circulation . Journal of Computational Physics 105, 333–338.